CLICdet: The post-CDR CLIC detector model

N. Alipour Tehrani[*], J.-J. Blaising[†], B. Cure[*], D. Dannheim[*], F. Duarte Ramos[*], K. Elsener[*],

A. Gaddi[*], H. Gerwig[*], S. Green[‡], C. Grefe[§], D. Hynds[*], W. Klempt[*], L. Linssen[*],

N. Nikiforou[*], A. Nurnberg[*], J.S. Marshall[‡], M. Petric[*], S. Redford[*], P. Roloff[*], A. Sailer[*],

F. Sefkow[¶], E. Sicking[*], N. Siegrist[*], F. Simon[‖], R. Simoniello[*], S. Spannagel[*], S. Sroka[*],
L.R. Strom[*], M.A. Weber[*]

[*] *CERN, Geneva, Switzerland,* [†] *LAPP, Annecy, France,* [‡] *Cavendish Laboratory, University of Cambridge, Cambridge, United Kingdom,* [§] *University of Bonn, Germany,* [¶] *DESY, Hamburg, Germany,* [‖] *Max-Planck-Institut fuer Physik, Munich, Germany,* [**] *now at PSI, Villigen, Switzerland*

Abstract

A new model for the CLIC detector has been defined based on lessons learnt while working with the CDR detector models and after a series of simulation studies. The new model, dubbed "CLICdet", also incorporates the experience from various R&D activities linked to a future experiment at CLIC. This note describes the studies and thoughts leading to the new detector model, and gives details on all of its sub-detector systems.

NB: This is a modified version of the CLICdp-Note-2017-001 - the changes, introduced on 5 April 2019, are listed in Appendix III.

1 Introduction

A state-of-the-art detector, built using cutting-edge technology and optimised through simulation, is crucial to exploit the physics potential of CLIC. Two detector models were previously defined, based on concepts for the ILC detectors and adapted for the higher centre-of-mass energies at CLIC. The CLIC_ILD [1] and CLIC_SiD models [2] were used in the CDR [3] and physics studies in 2013 and 2014. Based on the lessons learnt during these years as well as the experience from several additional optimisation studies, a new model, dubbed CLICdet, has been designed for the forthcoming physics benchmark studies. This note presents the version of CLICdet as defined in spring 2017.

The physics requirements and the experimental conditions (beam-beam effects and backgrounds) are most challenging at the highest collision energy. Therefore, similarly to the CDR studies, the focus of this detector optimisation work is on 3 TeV CLIC. As a result, this note describes the new 3 TeV CLIC detector model. The crossing angle between the colliding beams is 20 mrad at 3 TeV. For the initial stage of CLIC (380 GeV in the present staging scenario [4]) the innermost and very forward region of the detector will have to be designed differently (due to a smaller crossing angle, and due to less incoherent electron-positron pair background allowing for a smaller radius of the first vertex barrel layer). The changes in the detector layout are significant, but not very complex – engineering details of the detector model for lower energy CLIC operation will be studied at a later stage.

In chapter 2, this note provides details on the working hypotheses while chapter 3 gives an overview of the overall detector dimensions and most important parameters. Chapters 4 and 5 describe the vertex detector and the silicon tracker system. The electromagnetic and hadronic calorimeters are described in chapters 6 and 7, while chapter 8 gives details of the magnet system (solenoid and yoke) as well as the muon detectors. The very forward region is described in chapter 9, and the beam pipe and vacuum system is discussed in chapter 10. Chapter 11 recapitulates the detector opening and maintenance scenarios, which are very similar to those described in the CDR. Finally, Appendix I contains a table with the sensor areas of each sub-detector system, the pixel/pad sizes and the resulting total number of channels.

Throughout this note, the term "fast simulation" refers to the use of the LiC Detector Toy [5], while "full simulation" refers to detector simulations using GEANT4. Where "overlay of background" is mentioned, this refers to background events from $\gamma\gamma \rightarrow$ hadrons interactions stemming from 60 bunch-crossings.

2 Working Hypotheses

A number of detector design issues, and some matters concerning the layout of the CLIC experimental area, result from a complex interplay of CLIC accelerator optimisation and the envisaged CLIC physics reach. In order to make progress with the new CLIC detector model, it was inevitable to make some assumptions – these are here called "working hypotheses". Future detailed studies might lead to a revision of these assumptions.

2.1 A single detector at CLIC

Following the ILC model [6], the CLIC detector and physics studies were pursued for the CDR assuming the construction of two experiments, installed in a push-pull scheme. While the feasibility of such an arrangement was conceptually proven, it became clear that the two-detector scheme implies considerable extra cost, and beam time would inevitably be lost in the push-pull operations. Moreover, the results of benchmark analyses indicated that, with some exceptions in the forward direction, the physics reach was very similar for CLIC_ILD and CLIC_SiD.

In parallel, it also became evident that the CLIC beam and background conditions are not favourable towards a TPC (as planned in ILD), at least not at 3 TeV CLIC (see [7] and [8]). This, in turn, implied

that the possible two CLIC detector concepts would look remarkably similar.

In conclusion, and **as a first working hypothesis**, it was agreed to consider one detector only for the present studies. In order to retain a very compact layout of the installation around the interaction point (IP), the opening of the detector for maintenance and repairs is supposed to happen in a dedicated area in close vicinity of the IP ("garage position").

2.2 QD0 outside of the detector region

In the two CDR detector concepts for CLIC, the last quadrupole magnet of the accelerator (the QD0) was embedded in the detector. This layout choice was enforced to allow for the highest possible luminosities, generally obtained with a short distance L^* between the IP and the near end of the QD0 magnet. In analogy to the ILC case at that time, the two detector concepts did not have the same L^*: for CLIC_ILD, this distance was 4.3 m, for CLIC_SiD it was 3.5 m, mainly arising from the different overall length of the tracking detectors.

Integrating the QD0 within the complex forward region of the detectors was a challenge, which was further aggravated by the very stringent requirements to keep this magnet stable in position. In order to limit luminosity losses due to vibrations, the stability criterion was set to be less than 0.2 nm r.m.s. at frequencies above 4 Hz. This implied that additional space was required for a support tube and stabilisation systems. Together with the requirements for the opening of the detector for maintenance, the minimal support tube radius was found to be about 50 cm, resulting in a much reduced forward coverage of the hadron calorimeters in the CLIC CDR detector concepts.

During discussions within the CLIC detector and physics collaboration (CLICdp) and with accelerator experts, it became clear that it was impossible to assess, a priori, if the possible luminosity loss due to a longer L^* can be off-set by the potential gain in physics reach due to a better forward coverage. In both cases, rather complex detailed studies would be needed. Therefore, after studies of the magnet and yoke system with a possible reduction in overall detector length, it was decided – **as a second working hypothesis** – to move the QD0 to an L^* of 6 m, i.e. outside of the detector region. With such a layout, a significantly better forward HCAL coverage is possible, which is desirable given several important physics scenarios which require reconstruction of physics objects at low polar angles.

3 Overall Dimensions and Parameters

This chapter provides information about the general considerations leading to the choice of the main detector parameters such as tracker radius and magnetic field strength. A comparison to the CDR detector models is presented in Table 1. An illustration of the CLICdet model compared to CLIC_SiD is given in Figures 1 and 2.

Table 1: Comparison of key parameters of the different CLIC detector concepts. CLIC_ILD and CLIC_SiD values are taken from the CDR [3]. The inner radius of the electromagnetic calorimeter (ECAL) is given by the smallest distance of the calorimeter to the main detector axis. For the hadronic calorimeter (HCAL), materials are given separately for the barrel and the endcap.

Concept	CLICdet	CLIC_ILD	CLIC_SiD
Vertex inner radius [mm]	31	31	27
Tracker technology	Silicon	TPC/Silicon	Silicon
Tracker half length [m]	2.2	2.3	1.5
Tracker outer radius [m]	1.5	1.8	1.3
ECAL absorber	W	W	W
ECAL X_0	22	23	23
ECAL barrel r_{min} [m]	1.5	1.8	1.3
ECAL barrel Δr [mm]	202	172	139
ECAL endcap z_{min} [m]	2.31	2.45	1.66
ECAL endcap Δz [mm]	202	172	139
HCAL absorber barrel / endcap	Fe / Fe	W / Fe	W / Fe
HCAL λ_I	7.5	7.5	7.5
HCAL barrel r_{min} [m]	1.74	2.06	1.45
HCAL barrel Δr [mm]	1590	1238	1177
HCAL endcap z_{min} [m]	2.45	2.65	1.80
HCAL endcap Δz [mm]	1590	1590	1595
Solenoid field [T]	4	4	5
Solenoid bore radius [m]	3.5	3.4	2.7
Solenoid length [m]	8.3	8.3	6.5
Overall height [m]	12.9	14.0	14.0
Overall length [m]	11.4	12.8	12.8
Overall weight [t]	8100	10800	12500

3.1 Tracker volume radius vs. magnetic field

Transverse momentum resolution, angular track resolution and jet energy resolution using particle flow [9] benefit from a larger tracker radius. The dependence on tracker radius is stronger than that for a change in the magnetic field strength, as anticipated by the Gluckstern formula[1] [10]. Results from fast simulation are shown in Figure 3 for 500 GeV muons at $\theta = 90°$. A tracker radius of 1.5 m was chosen as a compromise between CLIC_SiD (1.3 m) and CLIC_ILD (1.8 m). (In fact, 1.5 m was later defined as the inner radius of the inscribed circle of the ECAL barrel, see Chapter 6). In a first stage, a magnetic field between 3.5 and 4.5 T was being discussed.

---

[1]The multiple scattering contribution to the track momentum resolution is proportional to 1/(BL). For variations of B and L considered in the options for the CLIC detector, the changes in the multiple scattering contribution are minor.
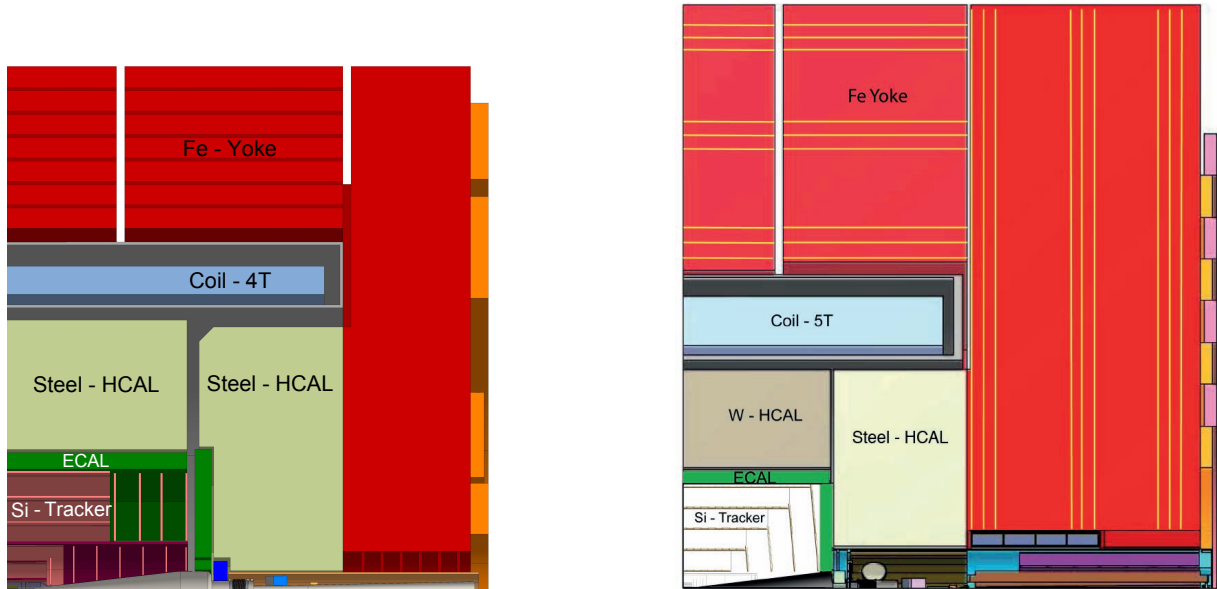
Figure 1: Longitudinal cross section showing the top right quadrant of CLICdet (left) and CLIC_SiD (right). In CLICdet, the structures shown on the right of the image (i.e. outside of the yoke) represent the end coils, while in CLIC_SiD these are a schematic illustration of shielding rings.
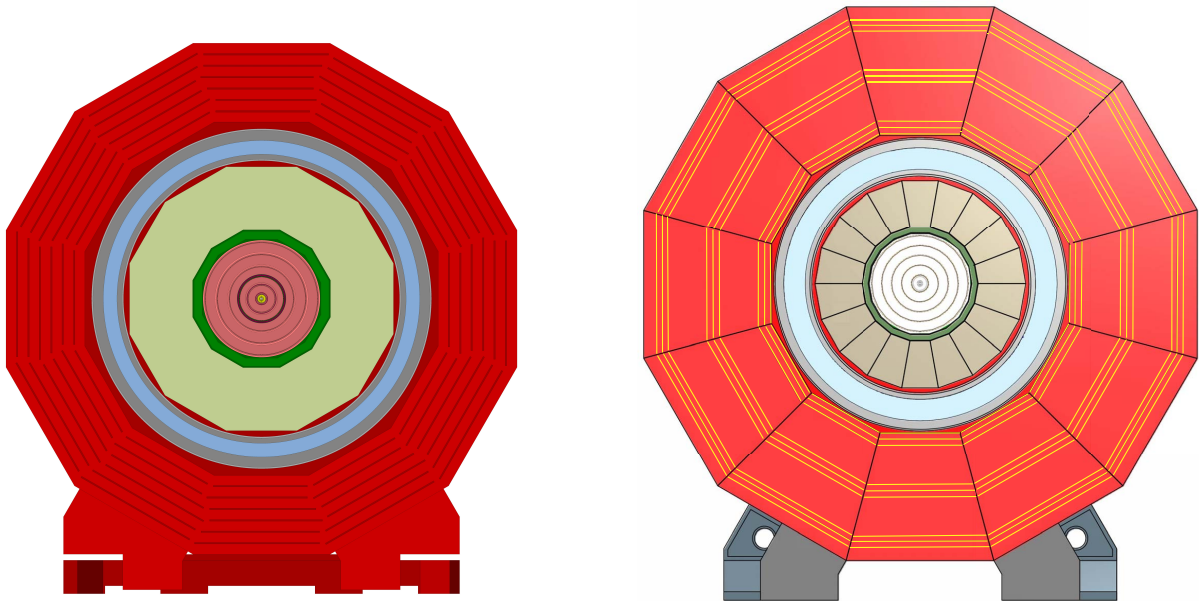

Figure 2: Transverse (XY) cross section of CLICdet (left) and CLIC_SiD (right).

3.2 Magnetic field vs. occupancies and flavour tagging

Occupancies in the vertex detector due to incoherent electron-positron pairs from beamstrahlung are directly affected by the magnetic field strength [11]. With an outer tracker radius of 1.5 m a magnetic field strength of 3.5 T would be sufficient to retain the transverse momentum resolution achieved with the CLIC_SiD concept. The bore of the solenoid would thus have a radius of around 3 m in case of a tungsten based HCAL, 3.4 m for an HCAL with steel absorbers. Such a free bore is similar to the CMS coil (but with a shorter coil, e.g. 8 m in CLIC_ILD vs. 13 m in CMS). Given these dimensions, a magnetic field strength of 4.5 T should be technically feasible. After investigating the impact of the magnetic field
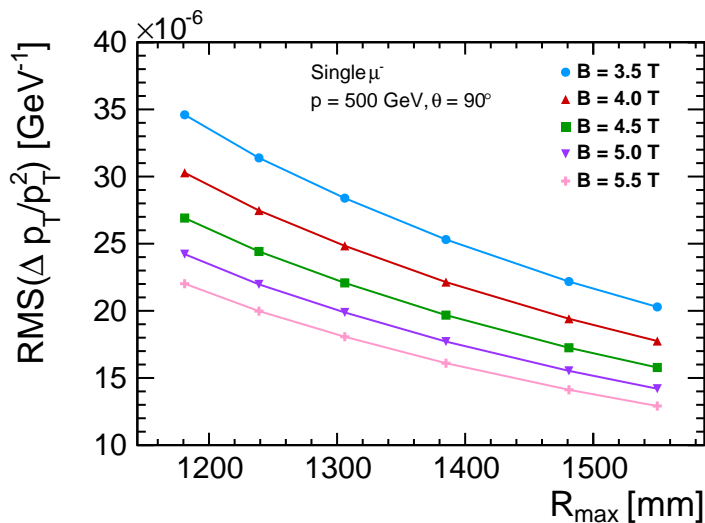
Figure 3: Momentum resolution as a function of tracker radius for different strengths of the B-field. Results obtained in fast simulation, for 500 GeV muons at θ=90° and for a silicon strip tracker with a point resolution of 7 μm. Note that at such high momenta, the contribution from multiple scattering is negligible.

strength on the pair background in the vertex detector, studies on the flavour tagging performance as a function of vertex innermost radius were performed - these showed a weak dependence [12]. Finally, following discussions with CMS engineers on magnet design feasibility and risks, the magnetic field strength for the new CLIC detector model was chosen to be 4 T.

3.3 Tracker volume length and tracker layout

A good acceptance in the forward region is particularly important for the higher energy stages at CLIC. A long main tracker is crucial for the forward tracking performance since the momentum resolution depends strongly on the lever arm at lower angles ($1/R^2$ for p_T and $1/L$ for the polar angle, see [10]). Here, R is the radius at which the particle leaves the tracker, $R < R_{max}$. By extending the tracker length, R and $\int BdR$ increases for the particles emitted in the forward direction.

Moreover, a longer distance from the IP to the calorimeter endcaps provides a better angular coverage of the hadronic calorimeter endcap. In the CDR detector models the angular coverage of the HCAL endcaps had been limited at their inner radius by the large support tube, which is not present in the new CLIC detector model.

A drastic reduction of the endcap yoke thickness, compensated by end coils, would a priori allow for an even longer tracking volume – however, the importance of an L^* of not more than 6 m and the on-axis B-field requirements in the region of the QD0 finally led to the value of 2.2 m (similar to the length chosen in CLIC_ILD) as the best compromise for the half-length of the tracker volume.

The layout of the silicon tracking layers was revisited. A CLIC_SiD style design would lead to outer tracker barrel layers of 4.4 m, was was found unrealistically long. A layout with a large support tube was chosen, separating the tracker volume into an inner and outer tracker region. Both regions consist of three barrel layers, complemented by seven and four forward tracker disks for the inner and outer tracker, respectively. The new layout is discussed in detail in Chapter 5.

3.4 Calorimeters

The work on ECAL for the new CLIC detector went through two distinct phases: during the earlier studies, emphasis was on jet energy resolution (with less attention paid to energy resolution for high energy photons). This led to an ECAL similar to CLIC_ILD, but with 25 instead of 30 layers (see Section 6.1).

Later, however, the importance of medium to high energy photons for CLIC physics was stressed, with a request for a sampling term of the energy resolution function smaller than 20%, and with a constant term as small as possible (the latter is crucially important for the very high energy photons). Optimisation studies found that a finer longitudinal sampling of the ECAL is needed to meet these requirements. An ECAL with 30 equally spaced layers marginally fulfills the requirements, but further improvements could be obtained with an ECAL of 40 layers. In conclusion, for the new detector model a silicon-tungsten (SiW) ECAL with 40 layers is chosen, with 1.9 mm thick W absorber plates, and with silicon sensor cells of 5×5 mm^2.

The HCAL depth remains at 7.5 λ_I, as required by physics studies for the CDR. Reducing the tracker radius (with respect to CLIC_ILD) and keeping the magnetic field at 4 T allows more radial space for the HCAL opening up for the possibility of using steel absorber plates instead of the more expensive tungsten. Further detailed studies, described in Chapter 7, have shown that the performances of a W-HCAL are not superior to those of a Fe-HCAL of the same depth in λ_I. As a result, steel is foreseen as absorber material for CLICdet in both the endcap and barrel region. The required inner bore radius for the solenoid is 3.5 m.

However, the decision to opt for a Fe-HCAL also has implications on the size, and thus the cost of the magnet system. The required bore radius increases by 0.37 metres when compared to the option of a W-HCAL. According to the parametric model developed in [13], this corresponds to an additional cost for the total magnet system (incl. the yoke) of about 25 MCHF. However, this must be compared to the cost of tungsten plates for a barrel HCAL (these were estimated to amount to 112 MCHF for CLIC_ILD and 60 MCHF for CLIC_SiD). Finally, the choice of a Fe-HCAL and thus the larger radius changes the aspect ratio and thus slightly impacts the inhomogeneity of the magnetic field in the tracker region. The change from aspect ratio 1.07 (for CLICdet with its Fe-HCAL) to 1.20 (had a W-HCAL been chosen) is deemed to be of minor importance.

Engineering considerations lead, at this stage of the conceptual detector design, to 12-fold calorimeter cross sections throughout. Discussions on cable routing from the inner detectors and calorimeters out through the yoke region lead to the layout shown in Figure 1 (left): The ECAL barrel is aligned with the HCAL barrel, and the ECAL endcap is inserted into the HCAL endcap to allow for a free vertical passage for cables and other services. Moreover, the inner top corner of the HCAL endcap is modified for a smooth passage of the services (90° angles are not feasible for services routing when little space is available).

Details of the optimisation studies for ECAL and HCAL are described in Chapters 6 and 7.

3.5 Magnet system

The magnet system of CLICdet consists of a superconducting solenoid producing a 4 T field in the centre of the detector, and a steel return yoke. Given that there is only one detector, the requirements on stray fields and radiation shielding [14] can be relaxed, leading to a reduced thickness of the yoke. The overall dimensions of the magnet system are shown in Figure 4. Also shown in the figure are the end coils, which are necessary to compensate for the reduced thickness of the yoke endcap w.r.t. the ILD magnet system [15]. Details of the magnet system are described in 8. Contrary to the CDR, there appears to be no need for an anti-solenoid [16][2] as a consequence of placing the QD0 outside of the detector region.

---

[2]In the CDR detector models, such an anti-solenoid needed to be introduced to shield (partially) the beam and the QD0 against the field from the detector solenoid.
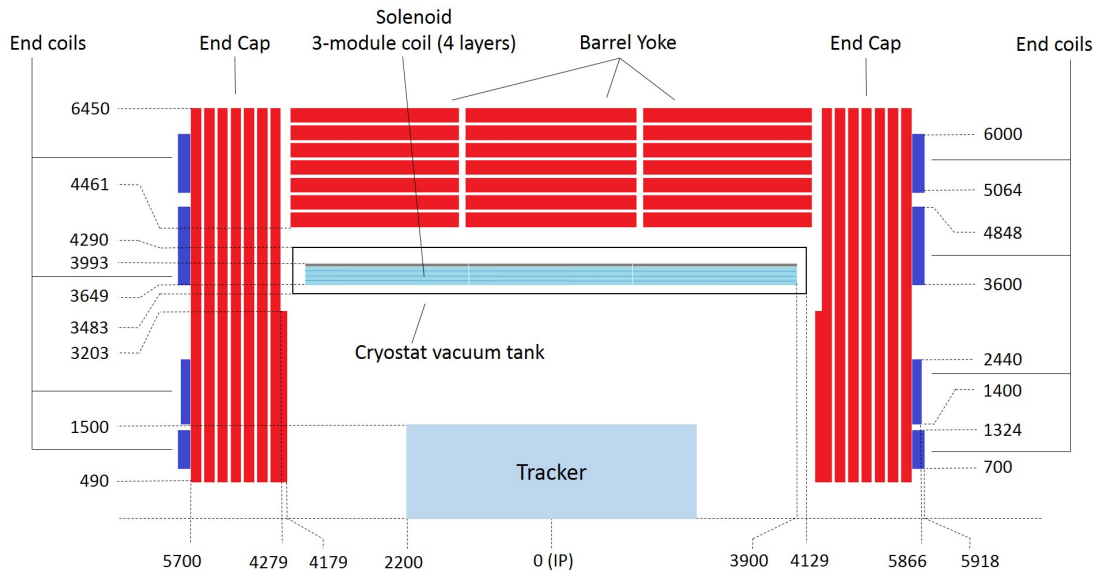
Figure 4: Schematic RZ view of the CLICdet magnet system. All dimensions are given in mm. To simplify the drawing, only one half of the magnet section is shown and calorimeters as well as other detector details are omitted.

3.6 Muon detectors

For engineering reasons, a minimal thickness of the iron plates in the return yoke of about 10 cm is required. Reducing the yoke endcap thickness therefore implies that the number of muon detection layers has to be reduced. In CLICdet, there are 6 muon detection layers (as compared to 9 in the CDR models). These 6 layers are distributed with equal spacing in the yoke. In the barrel region, and in analogy to the CDR detector models, an additional muon detection layer as close as possible to the solenoid is foreseen.

3.7 Very forward region

The main elements of the very forward region of CLICdet, containing the LumiCal and BeamCal detectors, remain as in the CDR models. The notable exception is the absence of the QD0 in the detector volume - this allows to simplify the vacuum system. Contrary to the CDR detector models, no vacuum valve is needed inside the detector volume (a large valve near LumiCal added considerable complexity in the CDR layout). The layout of the forward region is shown in Figure 5. Further details on the forward region, the vacuum system and the detector opening scenario are given in Chapters 9 to 11.
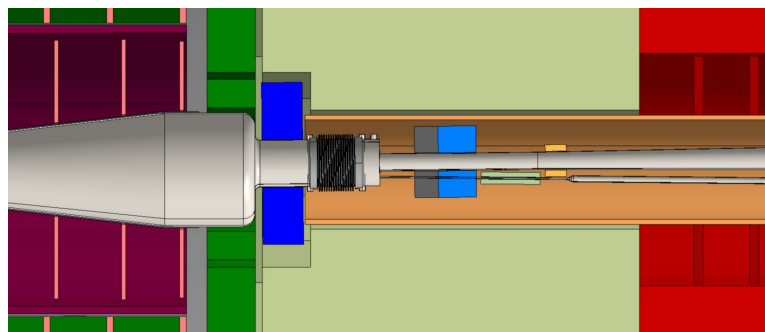

Figure 5: Layout of the forward region in CLICdet, seen from the top. The LumiCal is shown in dark blue, the BeamCal in light blue colour.

4 Vertex Detector

The vertex detector in CLICdet, similarly to the CDR detector models, consists of a cylindrical barrel detector closed off in the forward directions by "disks". The layout is based on double layers, i.e. two sensitive layers fixed on one support structure, in both barrel and forward region. The barrel consists of three double layers. In the forward region, the three "disks" are split up in 8 segments which are arranged to create a "spiral". This spiral geometry allows efficient air-flow cooling of the vertex detector [17]. The air-flow imposes that both spirals have the same sense of rotation - this leads to an asymmetric layout of the vertex "disks". An illustration of the vertex detector surrounding the vaccum pipe is shown in Figure 6.
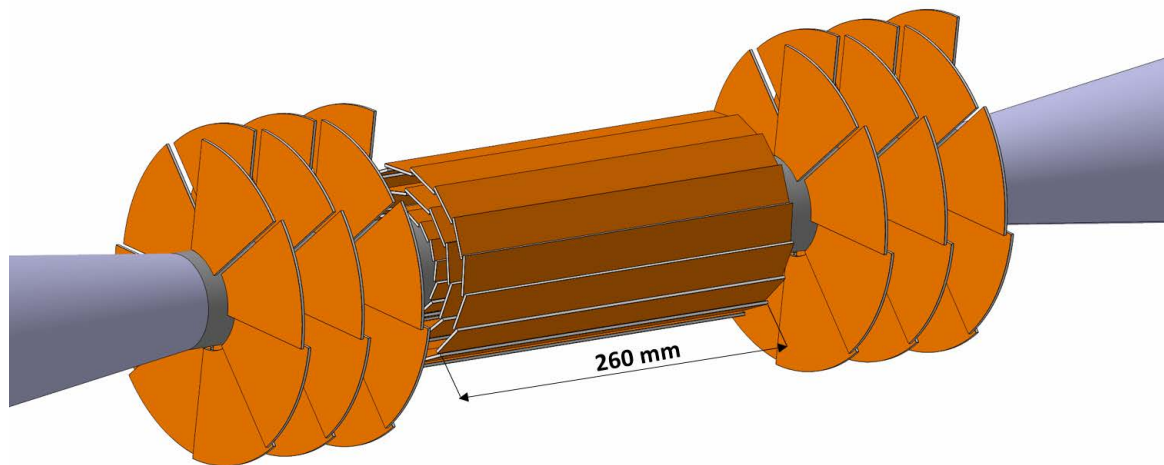

Figure 6: Schematic view of the CLIC vertex detector consisting of three double layers in the barrel and forward region spirals.

The material budget envisaged is 0.2% X_0 per detection layer (0.4% X_0 per double layer). The CLIC-det vertex detector is built from $25 \times 25\ \mu m^2$ pixels. Using pulse height information on charge sharing, a single point resolution of 3 μm is aimed for.

The inner radius of the innermost vertex barrel layer is limited by the occupancy from incoherent pairs. Along with the choice of the magnetic field of 4 T the inner radius has been increased from 27 mm (in CLIC_SiD) to 31 mm. The impact on the flavour tag performance due to this change is less than 10%, as shown in Figure 7, and is considered acceptable.

The overall length of the barrel vertex detector, built from staves, is 260 mm. The total area of the sensors in the three barrel double layers is 0.487 m^2. The double layer structure is shown in Figure 8, in the two options presently available in the simulations. Further details on the dimensions of the vertex detector barrel layers used in the simulation model are given in Table 2.

The eight petals per "disk" of the spirals (24 petals in total per side) are flat trapezoids installed at 90° to the detector axis. The first petal is located at Z = 160.0 mm from the interaction point, the last petal at Z = 298.8 mm. The longitudinal distance between the individual petals is 5.5 mm. In radial direction, the petals cover the range R = 33 mm to R = 102 mm (centre of the trapezoid base). The inner edge of the petals is 28 mm long, the outer edge measures 85 mm. These dimensions lead to an overlap of 2 mm from petal to petal. An overview of the vertex petal arrangement as implemented in the simulation is shown in Figure 9. The total area of the silicon sensors of all petals is 0.351 m^2.

In order to reach the very low material budget required, each sensor layer is built from 50 μm thick
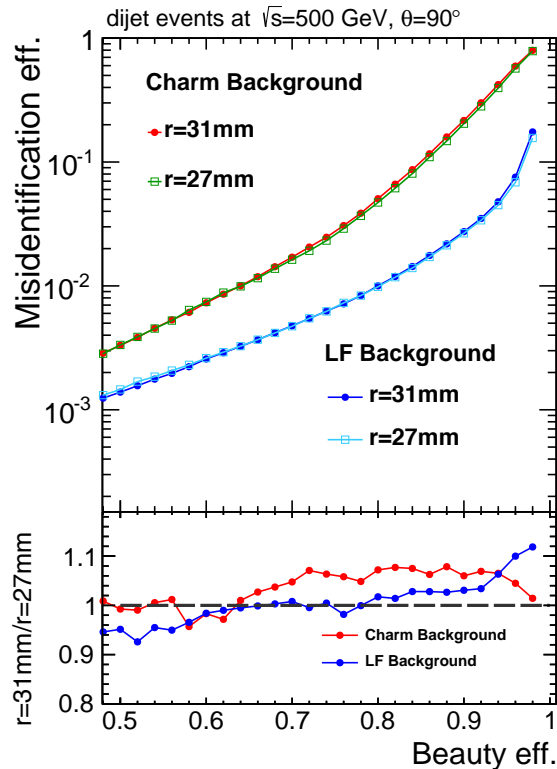
Figure 7: Comparison of flavour tag performance for two different radii of the innermost layer of the vertex detector (from [18]). Note that in this study, the magnetic field remained unchanged at 5 T.

Table 2: Vertex barrel layout as implemented in the simulations.

Barrel layers	Inner radius [mm]	No. of staves	Stave width [mm]
1 - 2	31 - 33	16	13
3 - 4	44 - 46	12	26
5 - 6	58 - 60	16	26

sensors attached to 50 μm thick ASICs. A central structure, consisting of a 1800 μm thick Rohacell glued inside two 30 μm thick CFRP skins, supports two such sensor+ASIC assemblies, thus forming a double-layer. On the outer side of each ASIC, 300 μm are foreseen for a combination of connectivity and power pulsing. The total thickness of the assembly is 2.8 mm. The support structure for the vertex petals needs to be stronger and is thus re-enforced with two additional CFRP skins, and a slightly thinner Rohacell core, resulting in the same assembly thickness as for the barrel layers. Details of the conceptual engineering design for the vertex layers can be found in [19].

A simplified layout is implemented in the simulation model. The 50 μm silicon sensors are separated by a 2 mm air-gap. On the outside of each sensor, an additional 140 μm of silicon represents the combined material of ASIC, support structure, connectivity and power pulsing. The resulting material budget corresponds to the thickness in X_0 in the engineering design, and is summarized in Table 3.

Air-cooling of the vertex detector, which is possible thanks to the reduced power dissipation reached using power-pulsing, has been extensively studied in simulations as well as in wind-channel and mock-up tests [17, 20]. The air needs to be guided from the outside of the CLICdet through piping to the central area of the detector, and out again on the opposite side. Moreover, since a sufficient cooling efficiency is

Table 3: Vertex detector double layer material budget as implemented in the simulations.

Function	Material	Thickness Barrel layers [μm]	Material budget Barrel layers [%X_0]	Thickness Petals [μm]	Material budget Petals [%X_0]
ASIC, support etc.	Silicon	140	0.149	170	0.181
Sensor	Silicon	50	0.053	50	0.053
Gap	Air	2000	0.001	2000	0.001
Sensor	Silicon	50	0.053	50	0.053
ASIC, support etc.	Silicon	140	0.149	170	0.181

(a) Option 1 - considered feasible from an engineering point of view

(b) Option 2 - presently used in the simulation model, but disfavoured from an engineering point of view
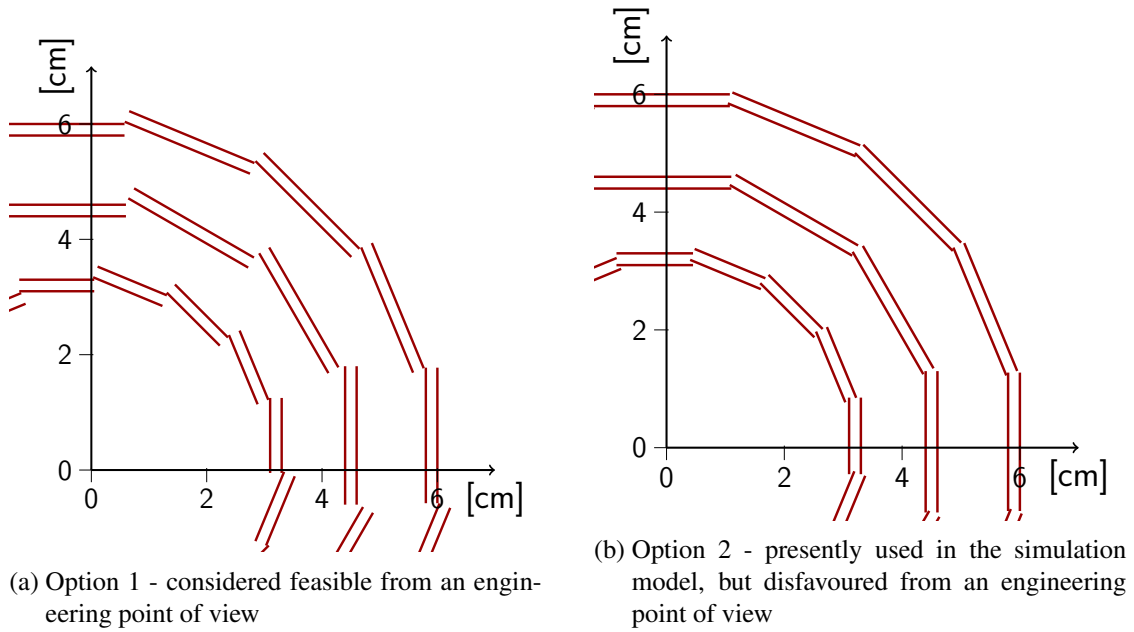
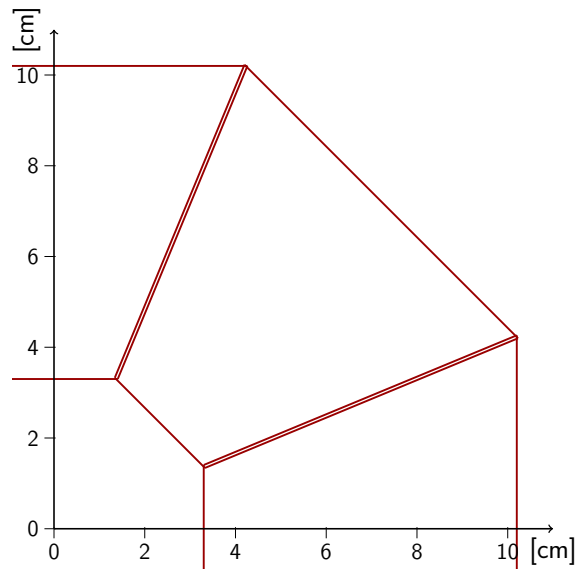Figure 8: The double layer arrangement in the vertex barrel detector (XY view).

Figure 9: Schematic view of the vertex forward petals arrangement, showing the 2 mm overlap between subsequent petals (XY view).

only achieved with a spiralling air-flow around the vertex detector barrel layers, the air must arrive at the vertex forward petals already with a rotational velocity component. Guiding the air to the vertex detector is achieved by a double-walled structure. The inner wall is the conical beam pipe made of 4.8 mm thick stainless steel, the outer wall consists of a < 1 mm CFRP sheet. A spiralling structure made of CFRP, inserted in the 5 mm space between the two walls, steers the air into a rotational flow. The layout as presently envisaged is schematically shown in Figure 10. In order not to limit the forward acceptance of the detector, a pointing geometry with the CFRP sheet limiting the aperture is chosen, with an angle of 6.6°. As a result, the half-length of the cylindrical (beryllium) part of the vacuum pipe is 308 mm (as compared to 260 mm in CLIC_ILD).
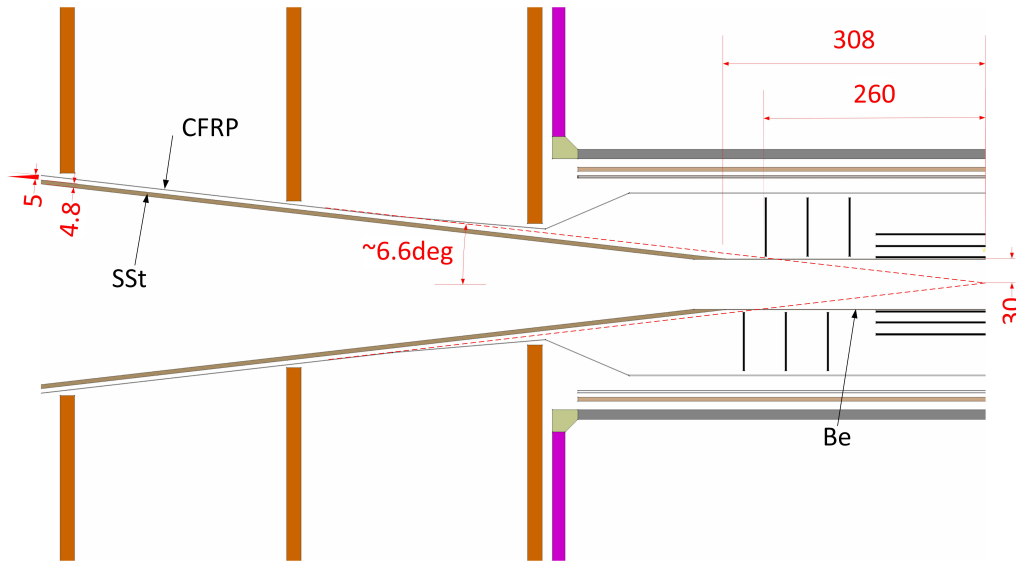

Figure 10: Engineering layout for the innermost region of the detector, indicating the conical beam pipe (stainless steel – SSt), and the outer shell (carbon-fiber-reinforced polymer – CFRP) used to create an air-channel for the vertex detector cooling. The positions of the vertex barrel and petal layers as well as the innermost tracker barrel layers and disks are indicated. A cylinder keeping the air flow in the close vicinity of the vertex detector is also shown.

5 Silicon Tracker

The tracking systems considered for the two CDR detector models were a TPC for CLIC_ILD and an all-silicon tracker for CLIC_SiD. Occupancy studies using the CLIC 3 TeV beam conditions [7, 8] found an occupancy of about 30% in the TPC pads (without safety factors), caused mainly by the long readout time and the fact that background hits are integrated over the full CLIC bunch train. Moreover, it turned out that the contribution of the TPC to an accurate momentum measurement is limited [3]. It was therefore concluded that the next CLIC detector model should feature an all-silicon tracker. As a result, the vertex and tracker are regarded as one unified tracking system in the reconstruction process. (The dimensions of the cells in vertex and tracker, as presently envisaged, are given in Appendix I 13.)

A conceptual design for supporting the vertex detector and beam vacuum tube inside a support cylinder had been proposed for the CDR detector models [21]. This support cylinder had a diameter just large enough to fit around the conical vacuum pipe. However, such a layout prevents the forward tracker disks to cover the smallest possible angles, thus penalising tracking in a region which is already suffering from the small $\int B$ dl. A support tube at a larger radius, as chosen for CLICdet, helps avoiding this issue.

The overall layout of the silicon tracker in CLICdet is shown in Figure 11. The tracking volume has a radius of 1.5 m and a half-length of 2.2 m. The main support tube has an inner and outer radius of 0.575 and 0.600 m, respectively, and a half-length of 2.25 m. This support tube effectively divides the tracker volume into two regions: the "Inner Tracker" and "Outer Tracker". The Inner Tracker contains three tracker barrel layers (ITB1-3) and, on each side of the barrel, seven inner tracker disks (ITD1-7). The Outer Tracker is built from three large barrel layers (OTB1-3) complemented on either side by four outer tracker disks (OTD1-4).

When compared to CLIC_SiD, CLICdet has a much larger tracking system, in particular extending the forward region acceptance. The number of expected hits in CLICdet as a function of polar angle θ is shown in Figure 12.
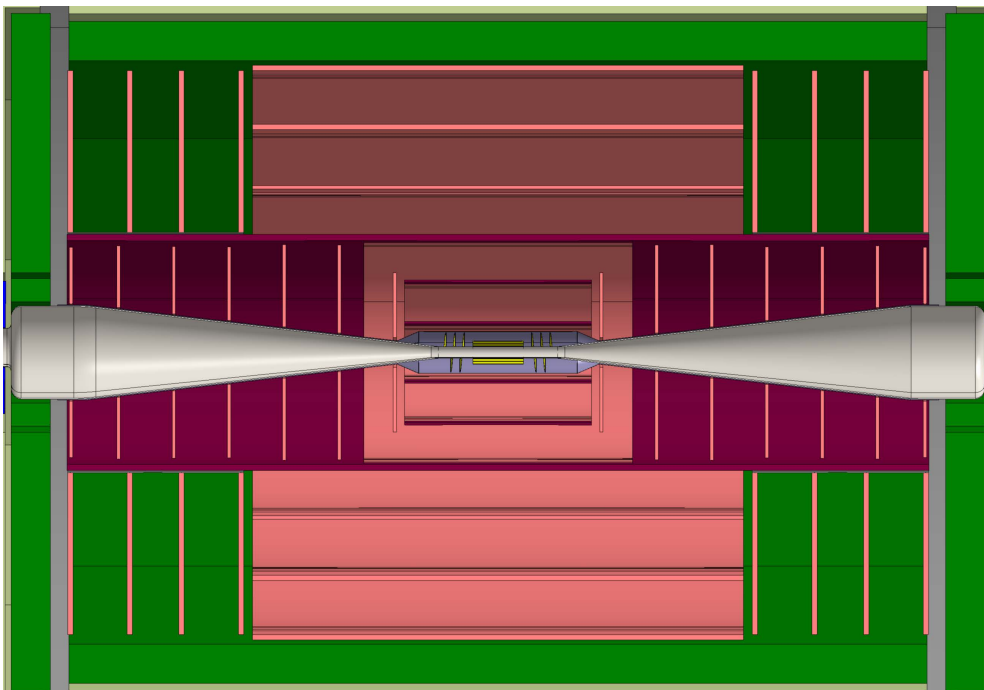

Figure 11: Overall layout of the tracking system: the area in darker red illustrates the main support tube for the inner tracking region, the vertex detector and the vacuum system. The central grey area is the envelope for the air cooling of the vertex detector.
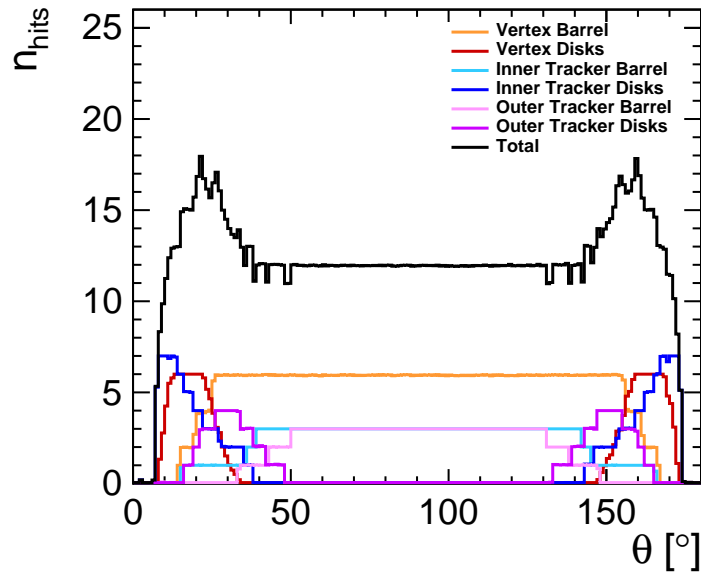
Figure 12: The coverage of the tracking systems with respect to the polar angle θ. Shown is the mean number of hits created by 500 GeV muons in full simulation. Only primary muon hits are taken into consideration (hits from secondary particles are ignored). At least eight hits are measured for all tracks with a polar angle down to about 8°.

Engineering studies are under way to define, in a preliminary manner, the support structures, cooling systems etc. needed for the tracker barrel layers and disks. The material budget needed in addition to the 200 μm thick layer of silicon (sensors plus ASICS or monolithic structure) can be estimated. In addition to the cylindrical main support tube, two carbon fibre structures ("interlink structures") are needed, to mount the inner and outer tracker barrel layers and to route connections. Only very preliminary sketches of these two interlink structures exist.

The building blocks from which the tracker detection layers are constructed, are modules of sensor plus ASIC. They are glued on one side to multi-layer carbon fiber structures acting as supports and containing the cooling. On the other side, these modules are glued to the elements needed for connectivity. In the tracker disks, modules are arranged into petals, which in turn are assembled into the full disks. In the inner and outer barrel, the silicon sensor size for all modules is 30×30 mm^2. Presently, an overlap between modules of approximately 2 mm is foreseen in radial direction - no overlap along the detector axis. The outer tracker disks are assembled from the same type of modules, 30×30 mm^2, while the inner tracker disks are made of modules with 15×15 mm^2 sensors. In all tracker disks, a considerable overlap between petals is foreseen while modules inside the petals have no overlap. Details of the present ideas on module support, overlaps etc. can be found in [19].

This preliminary engineering model is implemented in the simulation model of the tracker, with emphasis on the correct total material budget per layer (in X_0). The current implementation is shown in Figures 13 and 14. Simplifications with respect to the engineering model include the use of larger rectangular surfaces instead of the small modules in the tracker disk petals, as shown in Figure 15. The overall geometrical parameters of the tracker are given in Table 4 and 5 for the barrel and disks, respectively.

The material budget for the different tracker layers is listed in Tables 6 and 7. Details of the presently envisaged design can be found in [19]. The material budget for the modules (sensor and electronics) plus cooling and connectivity, is estimated to be 0.89% X_0 for ITB's and 1.02% X_0 for OTB's and tracker disks.

This material budget does not include the tracker support structures, made of carbon fibre components, which differs from layer to layer and amounts to 0.13% X_0 – 0.37% X_0. The CLICdet simulation model includes this additional material.

The main support tube, in its preliminary design, amounts to 1.25% X_0. The interlink structure for the outer barrel layers is estimated to contribute 0.3% X_0, while the inner interlink amounts to 0.5% X_0. Cables from the vertex detector, which are to be routed outwards along ITB1 and further out along the conical vacuum tube, are represented by an additional 0.47% X_0 (deemed to be a conservative estimate). In the CLICdet simulation model, both interlink structures are inserted with 0.6% X_0, approximately accounting for the actual graphite structure plus some of the cables. The total material budget for the vertex plus tracker region as a function of polar angle is shown in Figure 16.

Preliminary results of a first validation of the tracking in CLICdet are shown in Figure 17.

Figure 13: XZ-view of the tracker as implemented in the simulation model. The black lines indicate the tracker support structures including cooling and cables, the green lines represent the tracker sensor layers. The blue lines show the main support tube and the interlink structures. The orange line indicates the vacuum tube. The vertex detector is shown in the centre (in red). Cables going outwards from the vertex detector are represented in magenta.
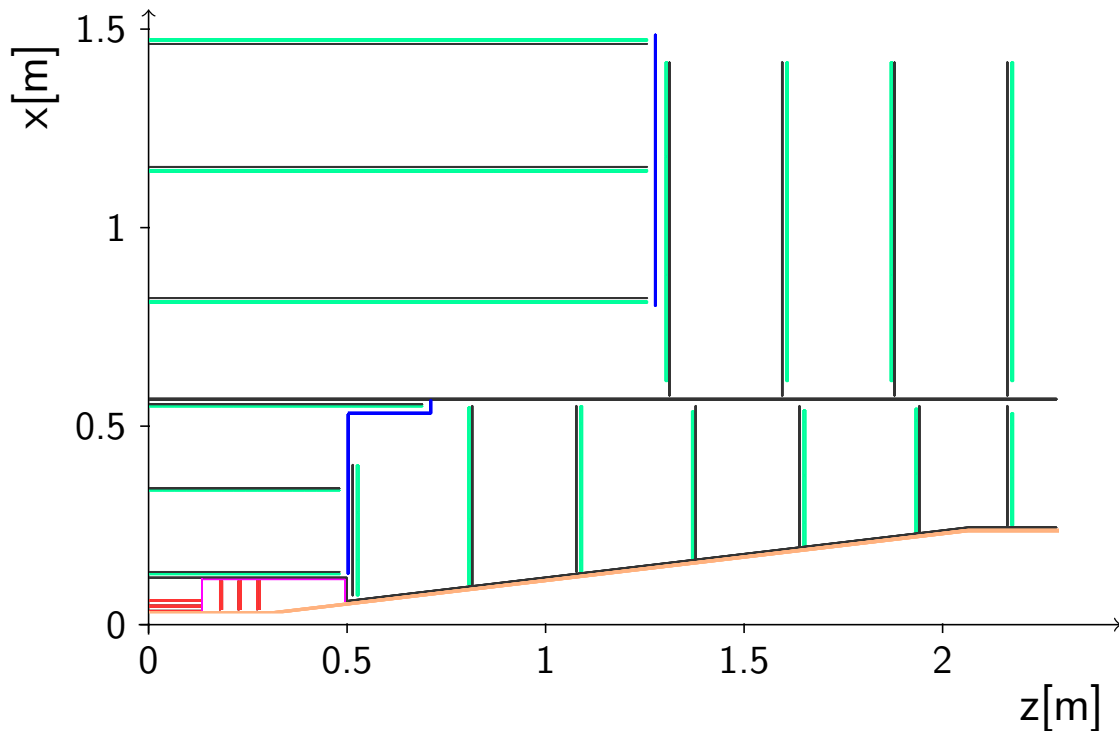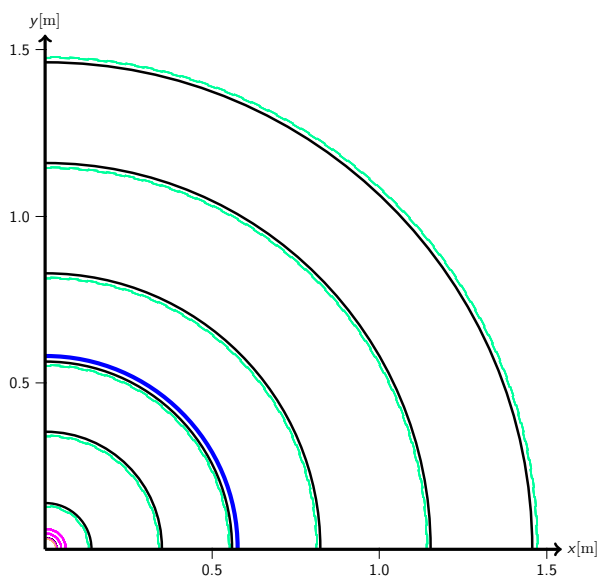
Figure 14: XY-view of the tracker barrel layers as implemented in the simulation model. The black lines indicate the support structures including cooling and cables, the green lines represent the tracker sensor layers. The blue line shows the main support tube. Vertex detector (in purple) and vacuum tube (in orange) are shown in the centre.
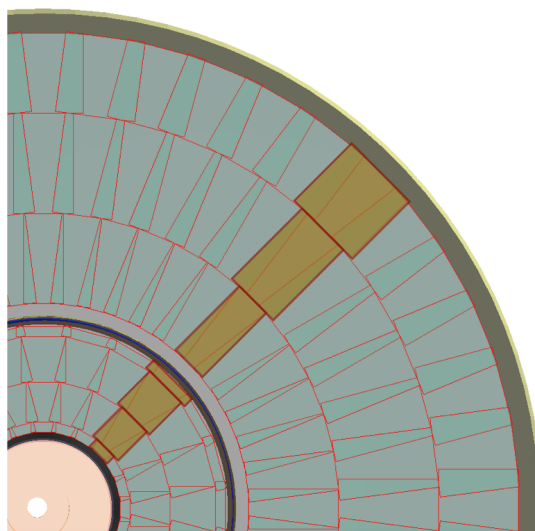
Figure 15: XY-illustration of the tracker disk implementation in the simulation model: the overlay between petals is visible as darker, smaller wedges. The petals are constructed from three (or four) rectangular volumes (example highlighted in yellow/brown), a simplification with respect to the engineering layout in [19]. N.B. This graph is a view from z = 1800 mm in downstream direction, thus showing the ITD6 and OTD3 inner and outer tracker disks.

Table 4: Main parameters of the tracker barrel layout, radius R and half-length L/2.

Layer No.	Name	R [mm]	L/2 [mm]
1	ITB1	127	482
2	ITB2	340	482
3	ITB3	554	692
4	OTB1	819	1264
5	OTB2	1153	1264
6	OTB3	1486	1264

Table 5: Main parameters of the tracker disks.

Disk No.	Name	Z [mm]	R_{in} [mm]	R_{out} [mm]
1	ITD1	524	72	404
2	ITD2	808	99	552
3	ITD3	1093	131	555
4	ITD4	1377	164	542
5	ITD5	1661	197	544
6	ITD6	1946	231	548
7	ITD7	2190	250	537
8	OTD1	1310	618	1430
9	OTD2	1617	618	1430
10	OTD3	1883	618	1430
11	OTD4	2190	618	1430

Table 6: Material budget of the tracker barrel layers - total per barrel layer, as implemented in the simulation.

Layer Name	X_0 [%]
ITB1 - 3	0.89
OTB1 - 3	1.02

Table 7: Material budget of the tracker disks - total per disk, as implemented in the simulation.

Disk Name	X_0 [%]
ITD1 - 7	1.02
OTD1 - 4	1.02
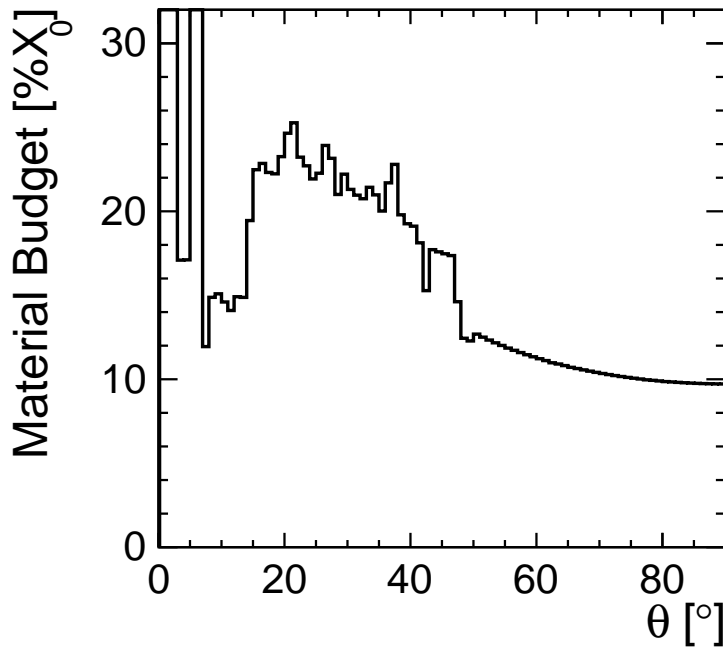
Figure 16: Total material budget of the vertex plus tracker system, including beam pipe, supports and cables, as a function of the polar angle.

17

Figure 17: Preliminary results of the momentum resolution as a function of particle momentum obtained with the CLICdet model (CLIC_o03_v08, head release of 2 Feb 2017). Single muons are passed through the full simulation and reconstruction chain of the CLIC software (simulation and reconstruction head release of 2 Feb 2017).

6 Electromagnetic Calorimeter

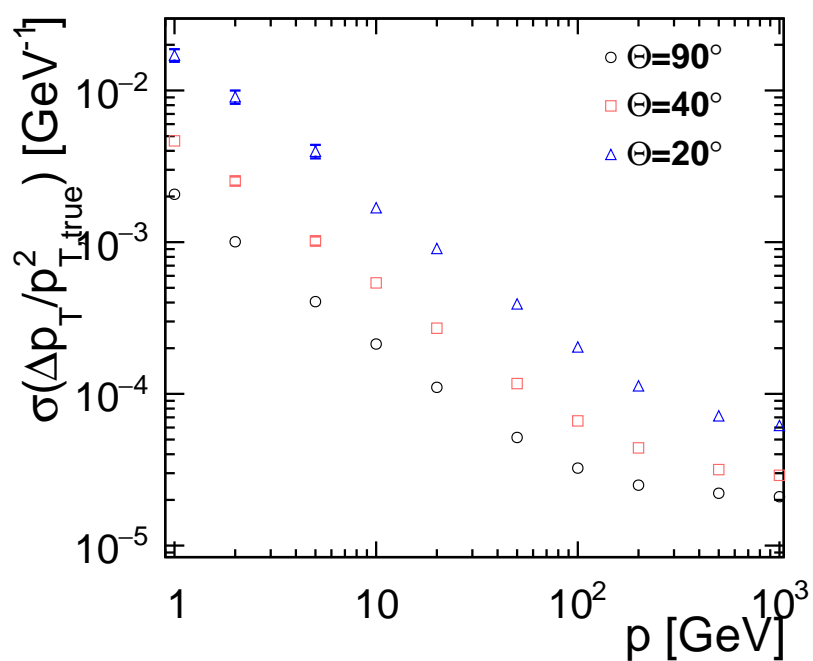Following the completion of the CDR, the detector optimisation efforts for the ECAL were pursued. The PANDORA particle flow algorithm has been used throughout. The work can be separated in two parts: (1) ECAL optimisation using the ILD detector model for ILC, with emphasis on jets, and with the paradigm that photon energy resolution is not expected to be a major physics driver, and (2) ECAL optimisation studies with a DD4hep based new CLIC detector model and the push for excellent energy resolution for high energy photons. The results of both approaches are summarized in this chapter – the second design philosophy was finally chosen for the new CLIC detector model.

6.1 ECAL optimisation with emphasis on jets

The initial round of ECAL simulation studies towards a new CLIC detector model was concluded as follows:

- It had been agreed previously that the inner radius of the ECAL should be 1500 mm.

- The ILD detector concept assumes 30 ECAL layers, with the silicon-tungsten[3] option considered the baseline. The optimal cell size was found to be 5×5 mm^2. Reducing the number of ECAL layers (while keeping a fixed ECAL thickness in X_0) results in a moderate increase of the sampling term in the photon energy resolution at lower energies. For example, the energy resolution for 10 GeV and 100 GeV photons as a function of the number of ECAL layers is shown in Figure 18. Furthermore, the electron energy resolution is mostly based on the track momentum resolution for all but the highest energy electrons. On this basis, it was felt that the penalty for reducing the baseline ECAL design from 30 to 25 layers would be acceptable. Accordingly, the number of layers for the two ECAL sections was set to 17 for the first part (thinner plates) and 8 for the second part (thicker absorber plates).

- The jet energy resolution is weakly affected by the lateral segmentation of the ECAL, as shown in Figure 19(a). The impact of larger cell sizes would need to be studied in more detail, e.g. for hadronic tau decays. Pending such additional studies, the baseline cell size of 5×5 mm^2 is kept as baseline. Similarly, the jet energy resolution only weakly depends on the number of ECAL layers (see Figure 19(b)).

- Using thin scintillators as active layers remains an option for a future CLIC detector, but the feasibility of a fine segmentation, the cost implications and calibration issues need to be understood in more detail.

6.2 ECAL optimisation with emphasis on high energy photons

Following the findings in the earlier round of studies, as presented in Section 6.1, the ECAL performance in terms of energy resolution for high energy photons was questioned. At 3 TeV CLIC, such photons are very important in a number of physics scenarios, e.g. for the measurement of Higgs decays, possible new heavy resonances, mass of dark matter candidates. For a recent overview, see [23]. Moreover, good ECAL performance is also crucial for the reconstruction of the luminosity spectrum using Bhabha events, since at the highest energies the ECAL resolution is better than the momentum resolution from the tracker [24].

In order to investigate the ECAL performance for different sampling options, a series of full simulation studies was performed [25]. Different ECAL models were simulated, as summarized in Table 8. Since

---

[3]In the simulations, the "tungsten" is a mixture of 93% tungsten, 6.1% nickel and 0.9% iron.
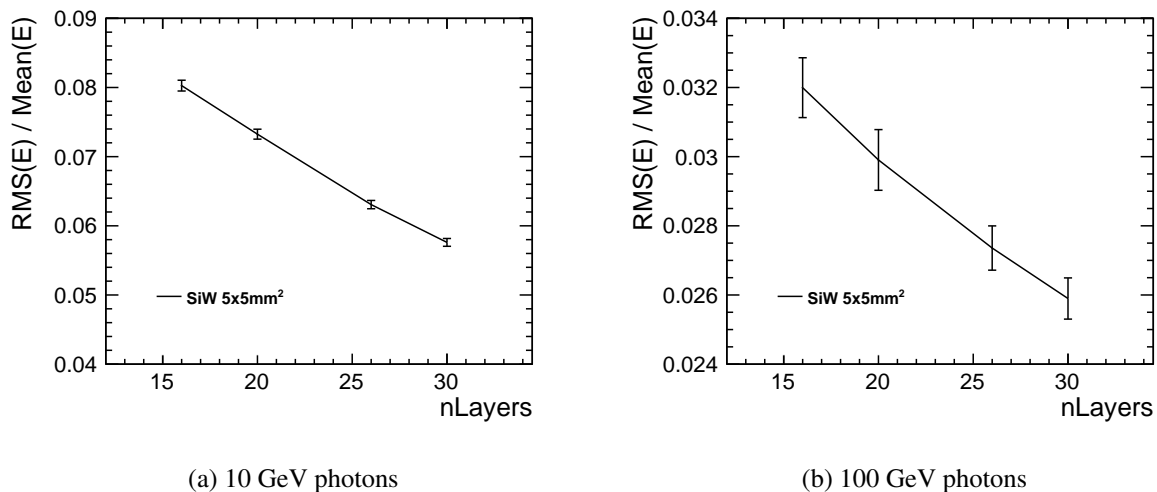
(a) 10 GeV photons

(b) 100 GeV photons

Figure 18: Silicon-tungsten (SiW) ECAL energy resolution in the ILD detector for 10 GeV and 100 GeV photons in the barrel, as a function of the number of ECAL layers. Error bars indicate the statistical accuracy of the simulation results. The total thickness of the ECAL is about 23 X_0, for all the cases shown (from [22], see Appendix II 14 for software details).

(a) as function of ECAL cell size
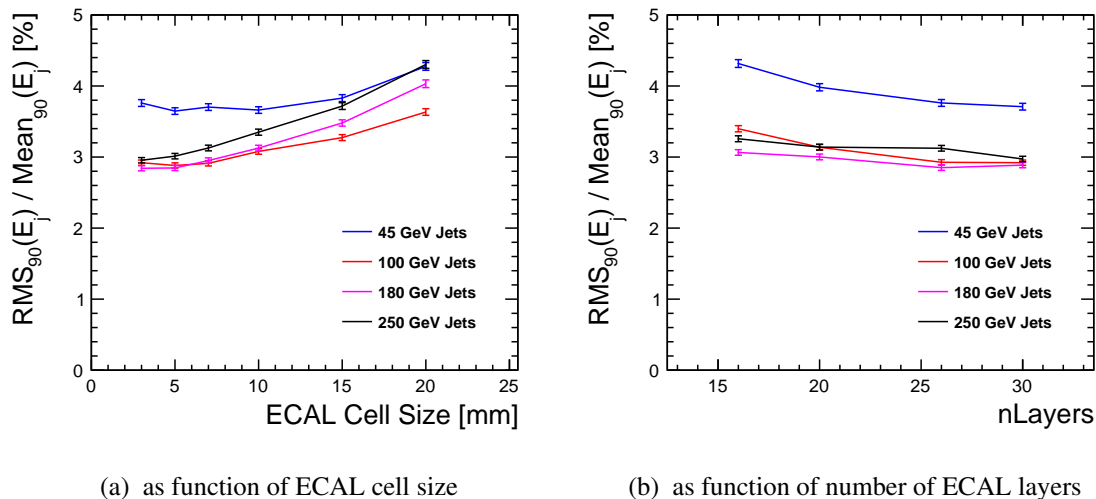
(b) as function of number of ECAL layers

Figure 19: Jet energy resolution in the ILD detector for jets of different energies, as a function of the SiW ECAL cell size and number of ECAL layers (keeping a constant depth of about 23 X_0). Error bars indicate the statistical accuracy of the simulation results (from [22], see Appendix II 14 for software details).

leakage into the HCAL was observed for high energy photons, a simultaneous ECAL and HCAL calibration using high energy photons was performed. A selection of simulation results, shown in Table 9, illustrates the main findings. The total energy resolution (from ECAL plus HCAL) as a function of photon energy is shown in Figure 20, for photons hitting the ECAL in the centre of the barrel (θ=90°, ϕ=0°).

It is noted that CLICdet_17_8 indeed performs worse than an ECAL with 30 layers. Moreover, a 30-layer ECAL with uniform layer thickness (CLICdet_30) was found to give better resolution than the previous 30-layer ECAL assembled in two groups (CLICdet_20_10), with thinner layers first and thicker layers later. This is readily understood from the evolution of shower depth as a function of energy: At

Table 8: List of the different ECAL models studied.

Label of the model	Layer structure	Thickness tungsten alloy [mm]	Space for sensor and electronics [mm]	Total thickness per layer [mm]
CLICdet_17_8	17 thin + 8 thick	2.4 + 4.8	2	4.4 + 6.8
CLICdet_20_10	20 thin + 10 thick	2 + 4	2	4 + 6
CLICdet_30	30 uniform	2.65	2	4.65
CLICdet_40_a	40 uniform	1.9	2	3.9
CLICdet_40_b	40 uniform	1.9	3.15	5.05

Table 9: Photon energy resolution for different ECAL configurations as defined in Table 8, for photons hitting the central region of the ECAL barrel (θ=90°, ϕ=0°) . The sigma (from a fit to a Gaussian distribution) of the distribution (E_{ECAL}+E_{HCAL})/E is given in [%].

Energy [GeV]	10	50	200	500	1000	1500
CLICdet_17_8	5.90±0.05	2.89±0.02	1.64±0.01	1.14±0.01	0.816±0.006	0.675±0.005
CLICdet_20_10	5.36±0.04	2.66±0.02	1.46±0.01	0.981±0.007	0.711±0.005	0.600±0.004
CLICdet_30	5.43±0.04	2.44±0.02	1.230±0.009	0.790±0.006	0.572±0.004	0.485±0.004
CLICdet_40_a	4.58±0.03	2.07±0.02	1.050±0.008	0.673±0.005	0.491±0.004	0.403±0.003
CLICdet_40_b	4.72±0.03	2.11±0.02	1.077±0.008	0.707±0.005	0.537±0.004	0.438±0.003

higher energies the peak of the distribution is located deeper inside the ECAL, i.e. in the region with thicker tungsten plates in the model CLICdet_20_10. The detector models with uniform fine sampling and 40 layers with 1.9 mm tungsten plates were found to perform best. A slightly larger (but more realistic) space reserved for sensor and electronics slightly reduces the performance, as shown by the comparison of CLICdet_40_a and _b.
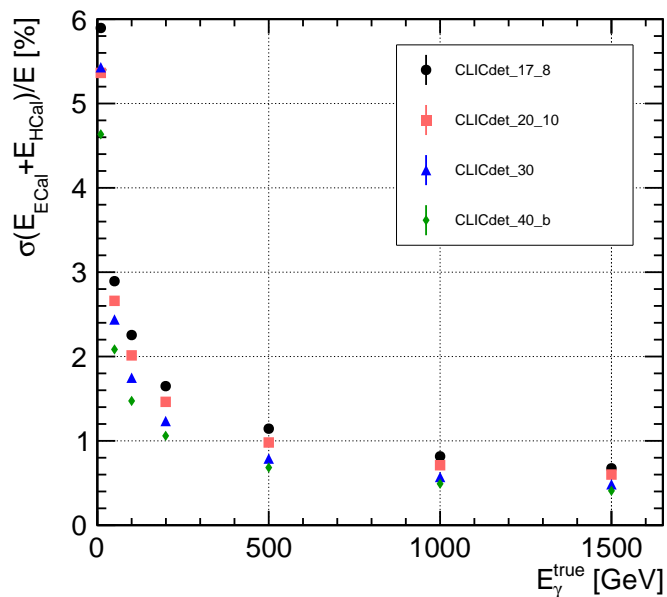
Figure 20: Resolution for high energy photons of the total ECAL plus HCAL energy, for different ECAL models as defined in Table 8. Photons are incident at θ=90° and ϕ=0°.

The energy resolution for the most promising model CLICdet_40_b was further investigated for photons uniformly distributed in the entire barrel region. Results are shown in Table 10. As expected, the resulting energy resolution is slightly worse than the one obtained in the (θ=90°, ϕ=0°) case.

Finally, using the software chain as given in Appendix II 14, the energy resolution studies for photons were also extended to the ECAL endcaps, again using CLICdet_40_b. The initial results showed that the reconstructed energy in the endcap was significantly lower than the one of the barrel. A scaling factor of 1.07 on the endcap response had to be introduced to match the response of the barrel. Detailed investigations into the causes of this difference revealed that the effect is due to the magnetic field, as described below.

Table 10: Photon energy resolution for the ECAL configuration CLICdet_40, with particles uniformly distributed in the entire barrel, compared to photons hitting the centre of the barrel. The sigma of the distribution $(E_{ECAL}+E_{HCAL})/E$ is given.

Energy [GeV]	50	500	1500
CLICdet_40_b entire barrel	2.28±0.02	0.955±0.007	0.775±0.006
CLICdet_40_b θ=90°, ϕ=0°	2.11±0.02	0.707±0.007	0.438±0.003

6.3 Impact of the B-field on the ECAL response

Investigating the detailed ECAL response for different polar angle regions, it was found that the barrel region gave a 7% higher raw hit energy sum than the endcap region, for all photon energies studied. Detailed studies revealed that the difference was not due to detector geometry, but is instead caused by the magnetic field: switching off the detector magnetic field moved the barrel response to the lower values found for the endcap. This observation was confirmed with photons using the full PFA reconstruction chain, as shown in Figure 21 for the case of 500 GeV. Aspects of the B-field effect on the e.m. shower development in ILD have been investigated earlier, see [26].
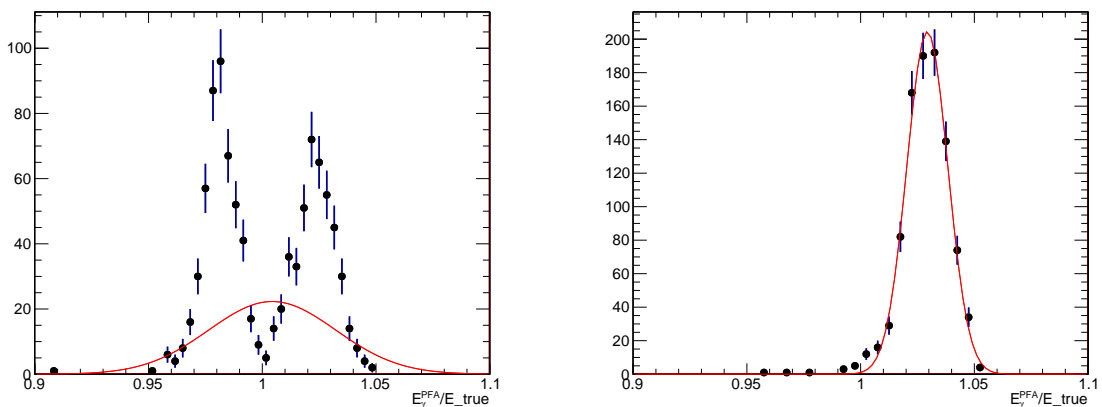
(a) Before correction - the left peak is endcap dominated, the right peak is barrel dominated.

(b) After correction - the response frome endcap and barrel overlap.

Figure 21: The ECAL response in the endcap-barrel transition region for 500 GeV photons, before and after the correction needed to compensate for the B-field effect.

6.4 Optimized ECAL layout as implemented in CLICdet

The basic ECAL structure of the CLIC detector is a silicon-tungsten sampling calorimeter with 5×5 mm^2 silicon detector cells. For improved photon energy resolution, in particular at high energy, the ECAL consists of 40 layers, with tungsten plates of 1.9 mm thickness and a distance of 3.15 mm between plates (i.e. the model CLICdet_40_b). The total thickness of the ECAL corresponds to about 22 X_0.

   The overall dimensions of the ECAL as implemented in the simulations are provided in Table 11. Opening the detector for maintenance or repairs, as described in Chapter 11, implies that the ECAL endcap has to be built in two parts, with a small so-called ECAL plug remaining in place attached to the support structures, while the bulk of the endcap is retracted. The necessary empty space between ECAL endcap and ECAL plug is presently assumed to be shaped as a ring, with a width of 30 mm.

Table 11: ECAL layout as implemented in the simulation model.

ECAL barrel r_{min} [mm]	1500
ECAL barrel r_{max} [mm]	1702
ECAL barrel z_{max} [mm]	2210
ECAL endcap/plug z_{min} [mm]	2307
ECAL endcap/plug z_{max} [mm]	2509
ECAL endcap r_{min} [mm]	410
ECAL endcap r_{max} [mm]	1700
ECAL plug r_{min} [mm]	260
ECAL plug r_{max} [mm]	380

   The ECAL segmentation as implemented in the simulation model is given in Table 12, and shown in Figure 22. Note that the ECAL starts with an absorber layer, followed by a sensor/electronics layer, and so on. The last element in the ECAL stack is a sensor/electronics layer.

Table 12: Parameters for the ECAL segmentation as implemented in the simulation model, with a total of 40 SiW layers.

Function	Material	Layer thickness [mm]
absorber	tungsten alloy	1.90
Insulator	G10	0.15
Connectivity	mixed (86% Cu)	0.10
Sensor	silicon	0.50
Space	air	0.10
PCB	mixed (82% Cu)	1.30
Space	air	0.25
Insulator	G10	0.75
Total between W plates		3.15
Total SiW layer		5.05
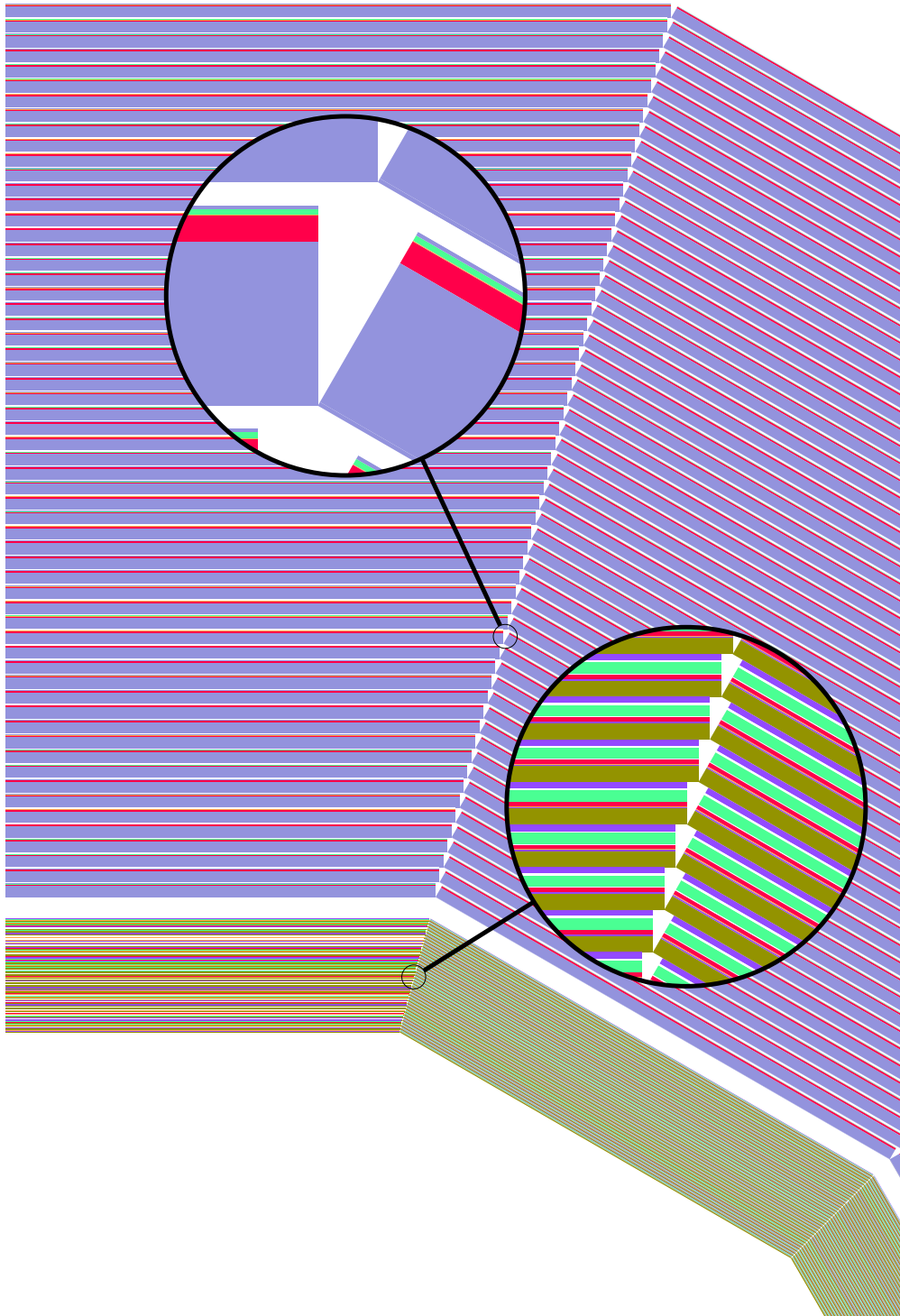
Figure 22: Implementation of ECAL and HCAL in the simulation model (the reader may need to zoom in to see all the details). The region of a junction between two sectors (of the dodecagon) in the barrel region is shown. In the ECAL, the olive-green regions indicate the tungsten layers, while the red regions symbolize the silicon sensors. Purple layers are G10, green is PCB and connectivity, and white is air. In the HCAL, blue regions indicate the steel layers (with thin steel sheets for the cassette), red stands for the scintillator, while green and white are PCB and air as in the ECAL.

7 Hadronic Calorimeter

Similarly to the case of the ECAL, detailed optimisation studies have been performed for the HCAL. Details are described in [27]. As an example result, Figure 23 shows the dependence of the jet energy resolution as a function of the number of layers in the HCAL (keeping the number of λ_I constant). The dependence of the jet energy resolution on the cell size in the HCAL is shown in Figure 24. Other parameters, such as the scintillator tile thickness, were varied but only a moderate impact on the jet energy resolution was found.
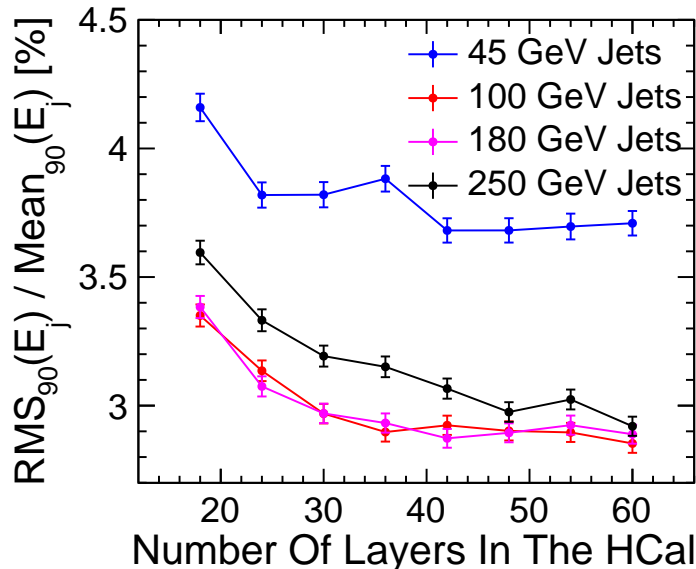

Figure 23: Jet energy resolution in the ILD detector for jets of different energies, as a function of the number of HCAL layers, keeping the number of λ_I constant.

As a result of these studies, the proposed hadronic calorimeter of CLICdet consists of 60 steel absorber plates, each of them 19 mm thick, interleaved with scintillator tiles, similar to the CALICE calorimeter design for the ILD detector. The gap for the sensitive layers and their cassette is 7.5 mm. The overall dimensions of the HCAL are summarized in Table 13. In the simulations, the part of the HCAL endcap which surrounds the ECAL endcap (see Figure 2) is treated as a separate entity called the "HCAL ring". The space needed to place the LumiCal inside the HCAL endcap is referred as "LumiCal cutout". The detailed segmentation parameters as implemented in the simulation model are given in Table 14. The polystyrene scintillator in the cassette is 3 mm thick with a tile size of 30×30 mm^2. Analog readout of the tiles with SiPMs is envisaged. Further details are presented in [27]. A section of the HCAL barrel as implemented in the simulations is shown in Figure 22.

Both, the endcap and the barrel HCAL, are around 7.5 λ_I deep, which brings the combined thickness of ECAL and HCAL to 8.5 λ_I (see Figure 25). In the studies performed in preparation of the CDR, this depth of the calorimetry for hadrons was found to be sufficient [28].

The overlap of m_W and m_Z measurements from the invariant mass of the two jets in WW $\rightarrow \nu \ell j j$ and ZZ $\rightarrow \nu \nu j j$ events, generated at various c.m. energies, is similar for a steel- and a tungsten-based calorimeter, as illustrated in Figure 26. The solid lines in the figure show the overlap for two different HCAL models, one using steel (blue) and the other using tungsten (red) as absorber material for identical λ_I, in the absence of beam-induced background. The dashed lines show the same measurements performed after the overlay of 60 bunch crossings of $\gamma\gamma \rightarrow$ hadrons background events generated at $\sqrt{s} = 3$ TeV. The overlap is used as an indication of the jet energy resolution (JER) obtained from each HCAL model.
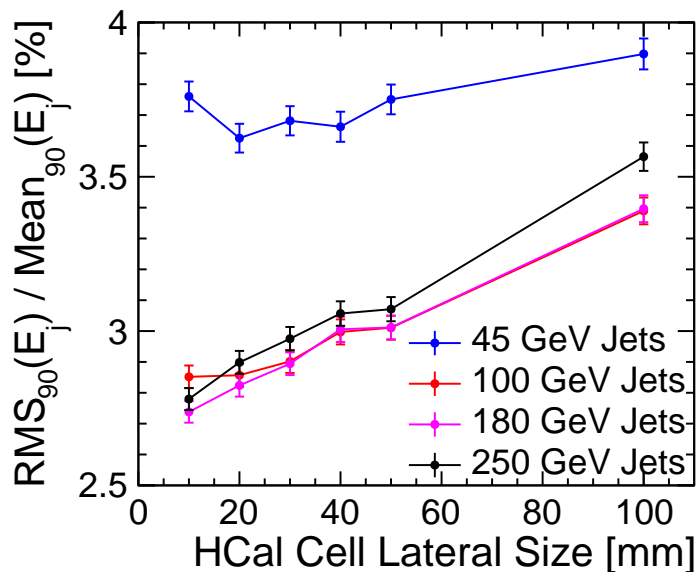
Figure 24: Jet energy resolution in the ILD detector for jets of different energies, as a function of the HCAL cell size. The cells are squared.

Table 13: HCAL overall layout as implemented in the simulation model.

|	
HCAL barrel r_{min} [mm]	1740
HCAL barrel r_{max} [mm]	3330
HCAL barrel z_{max} [mm]	2210
HCAL endcap z_{min} [mm]	2539
HCAL endcap z_{max} [mm]	4129
HCAL endcap r_{min} [mm]	250
HCAL endcap r_{max} [mm]	3246
HCAL ring z_{min} [mm]	2360
HCAL ring z_{max} [mm]	2539
HCAL ring r_{min} [mm]	1730
HCAL ring r_{max} [mm]	3246
LumiCal cutout in HCAL r_{max} [mm]	180
LumiCal cutout in HCAL z_{tot} [mm]	200

A larger overlap corresponds to a poorer separation between the W and Z invariant mass peaks which suggests a reduced JER. Since the performance of the two calorimeter options is very similar, steel was chosen as absorber material, for reasons of cost and complexity of machining and assembling of the tungsten plates.

Moving the QD0 outside of the detector region reduces the diameter of the support tube w.r.t. the CDR detector models. This in turn allows one to improve the forward coverage of the HCAL, which in CLICdet has an endcap inner radius of 250 mm.

As an illustration of the advantage of better forward coverage, a di-jet invariant mass measurement for jets in the forward region in $ZZ \rightarrow \nu\nu jj$ events for three HCAL models featuring different HCAL endcap inner radii has been performed in full simulations for several jet energies. For example, Figure 27 shows the results for physics events overlaid with 60 bunch crossings of $\gamma\gamma \rightarrow$ hadrons beam induced background. For reasons of computational efficiency, the ZZ were generated at $\sqrt{s} = 1$ TeV while

Table 14: Parameters for the HCAL segmentation as implemented in the simulation model, with a total of 60 Fe-Scintillator layers.

Function	Material	Layer thickness [mm]
Absorber	steel	19
Space	air	2.7
Cassette	Steel	0.5
PCB	mixed	0.7
Conductor	Cu	0.1
Scintillator	Polystyrene	3
Cassette	Steel	0.5
Total between steel plates		7.5
Total Fe-scint. layer		26.5
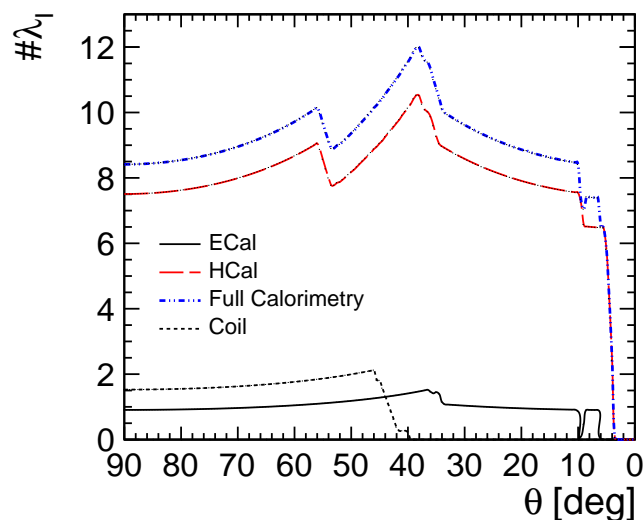
Figure 25: Nuclear interaction lengths λ_I in the calorimeters with respect to the polar angle θ. The interaction length corresponding to the material of the superconducting coil is shown for completeness.

the background events were taken from the worst case scenario, i.e. generated for CLIC operating at $\sqrt{s} = 3$ TeV. The k_t algorithm of FastJet was used to reconstruct exclusively two jets on the same side of the detector (after optimisation, the FastJet parameter R=0.5 and the "default" criterion for PFOs were used throughout to estimate the relative performance of the models) . The $R_{\text{in}} = 240$ mm model provides an improved di-jet invariant mass, without significantly increasing the acceptance to background compared to the $R_{\text{in}} = 360$ mm case. The $R_{\text{in}} = 120$ mm case, considered not feasible from an engineering perspective, is included for comparison.

While the advantage of a better HCAL forward coverage is evident even including the overlay of $\gamma\gamma \rightarrow$ hadrons background, detailed studies for CLIC_ILD revealed a too high occupancy in the inner regions of the HCAL endcap. As a remedy, a thick shielding (polyethylene and tungsten) inside the support tube was proposed [29]. In CLICdet, a shielding of this type would have to be placed inside the HCAL endcap and would therefore reduce its forward acceptance. For first physics studies with the new
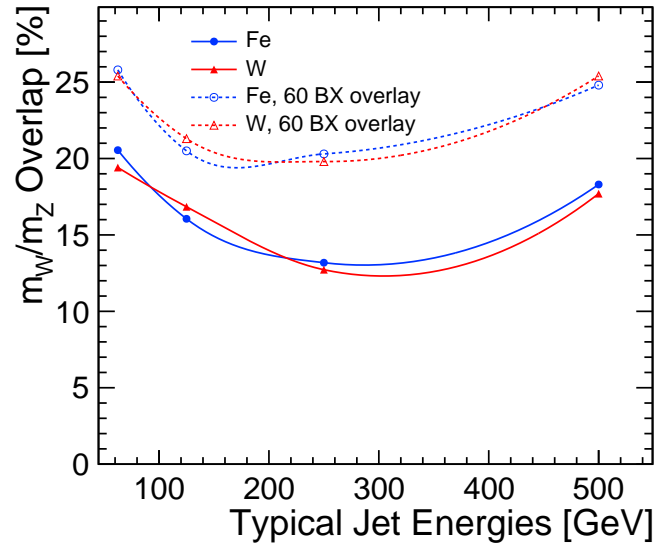
Figure 26: Overlap, in percent, of m_W and m_Z measurements from the invariant mass of the two jets in WW $\to \nu\ell jj$ and ZZ $\to \nu\nu jj$ events, respectively, as a function of the typical energy of the jets in the events. Solid lines show results without background events, dashed lines results with 60 bunch-crossings of $\gamma\gamma \to$ hadrons background overlaid.

detector model, it was decided not to include such a shielding. At a later stage, smaller sensor cell sizes in the forward HCAL, possibly combined with shielding, may have to be introduced.

Figure 27: Di-jet invariant mass measurement for jets in the forward region in ZZ $\to \nu\nu jj$ events for three HCAL models featuring different HCAL endcap radii.

28

8 Magnet System

8.1 Superconducting Solenoid

The solenoid magnetic field for the new CLIC detector model is chosen to be 4 T. This is understood to be a reasonable compromise between what is strictly ne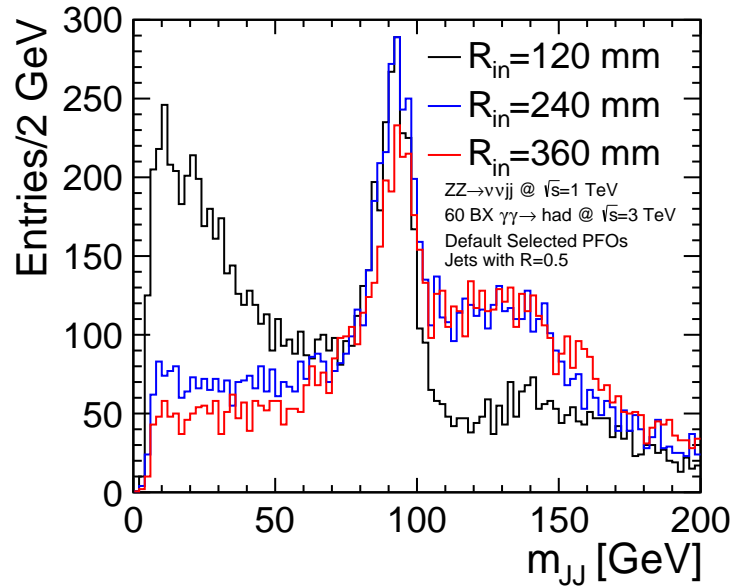cessary from the minimal requirements for tracking (3.5 T would be sufficient) and what is desirable, i.e. to have some margin in the detector performance while maintaining realistic solenoid parameters.

In the simulation model, the magnetic field in CLICdet is 4 T throughout the volume inside the superconducting coil. The field in the yoke is 1.5 T pointing in the opposite direction with respect to the inner field. Beyond the end of the coil the field decreases rapidly in Z-direction. Therefore, the simulation model currently assumes no field in the yoke endcap.

In the CDR, the design of the more challenging solenoid of CLIC_SiD, with smaller dimensions but a 5 T field, was described. The parameters of the solenoid for CLICdet are similar to the one of the ILD detector at the ILC, described in detail in [15]. The overall dimensions of the solenoid and yoke of CLICdet are shown in Figure 4.

At CLIC an anti-DiD dipole such as described for ILD is excluded: the luminosity loss due to synchrotron radiation by the beam in such a dipole field would be too large [30]. The main design parameters of the superconducting solenoid are given in Table 15. The solenoid of CLICdet is implemented in the simulation model with parameters as shown in Table 16. The material budget of the solenoid, in terms of λ_I, is indicated in Figure 25.

The solenoid for CLICdet is more challenging than the one of CMS, but is considered feasible using the technology available today. Due to the larger coil radius, the total magnetic flux in CLICdet is about 45% higher than the one in CMS. It was also noted during the discussions that the aspect ratio of the solenoid in CLICdet is not favourable to achieve a very homogenous field – however, external constraints (position of QD0) make it difficult to make the solenoid longer for the same diameter.

Table 15: CLICdet solenoid main parameters

Solenoid central field [T]	4.0	Nominal current [kA]	20
Maximum field on conductor [T]	4.6	Total ampere-turns solenoid [MAt]	29.8
Inductance [H]	11.6		
Coil inner radius [mm]	3649	Stored energy [GJ]	2.32
Coil outer radius [mm]	3993	Stored energy per unit of cold mass [kJ/kg]	12.9
Coil length [mm]	7800		

Table 16: Description of the coil elements as implemented in the simulation model. For all elements the material, the longitudinal extent in one half of the detector $z_{\min/\max}$ and the radial extent $r_{\min/\max}$ are given.

Material	$z_{\min}$ [mm]	$z_{\max}$ [mm]	$r_{\min}$ [mm]	$r_{\max}$ [mm]
Steel	0	4129	3483	3523
Vacuum	0	4129	3523	3649
Aluminium	0	3900	3649	3993
Vacuum	0	4129	3993	4250
Steel	0	4129	4250	4290
Vacuum	3900	4089	3649	3993
Steel	4089	4129	3483	4290

8.2 Yoke and Muon Detectors

The iron return yoke is structured into three rings in the barrel region and the two endcaps, as shown in Figure 28. The outer radius of the yoke is reduced w.r.t. the CDR detector models, since the external constraints (stray magnetic field, shielding) are relaxed in a scenario with only one detector. The yoke endcaps are much thinner than in the CDR to allow for an L^* of 6 m, with the QD0 outside of the detector region.
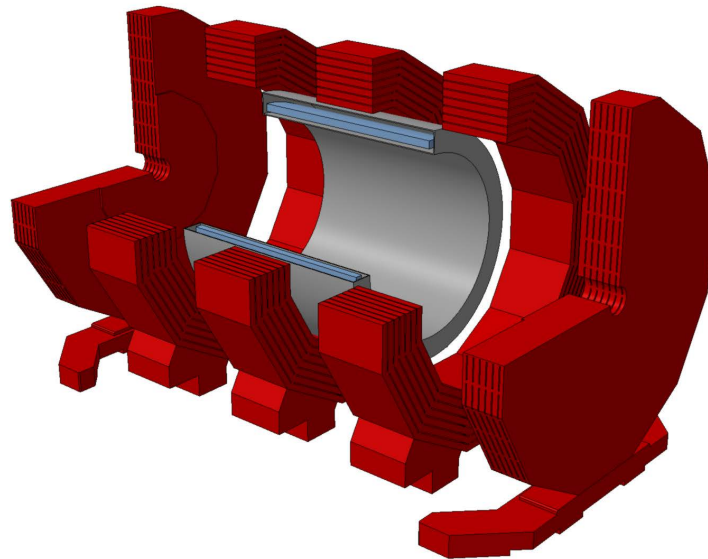

Figure 28: The iron return yoke of CLICdet. The end coils are not shown in this illustration.

In order to close the magnetic flux, a set of 4 concentric end coils is foreseen[4], as shown schematically in Figure 4. An earlier version of end coils is presented in [31], where the feasibility is demonstrated by a comparison with the coils used at the LHCb experiment. The main design parameters of the new end coils are given in Table 17. The effect of these end coils on the magnetic field outside of the detector region is shown in Figure 29. The peak value of the field decreases outside of the detector region ($z > 6$ m) when end coils are included, e.g. from about 0.5 T to 0.08 T at $z = 6.5$ m.

Table 17: Main design parameters of the four end coils per endcap. The dimensions of the coils are shown in Figure 4.

Coil	# turns	Copper mass [ton]	Resistance [mΩ]	Voltage drop [V]	Power [kW]
RC1	4×12	5.6	2.7	16.5	101
RC2	3×20	13.3	6.4	39.1	240
RC3	4×24	46.7	22.4	137.6	844
RC4	4×18	45.8	22.0	135.1	829

In the design of the yoke, mechanical constraints impose steel plate thicknesses of at least 100 mm. This implies that, in a thinner yoke, the number of muon detection layers needs to be reduced with respect to the CDR. Fewer muon layers are not expected to impair the performance of the muon identification at CLIC. This had already been anticipated in the note describing the design studies [32], which states that the "muon identification algorithm within PANDORAPFANEW leaves room for improvement". A

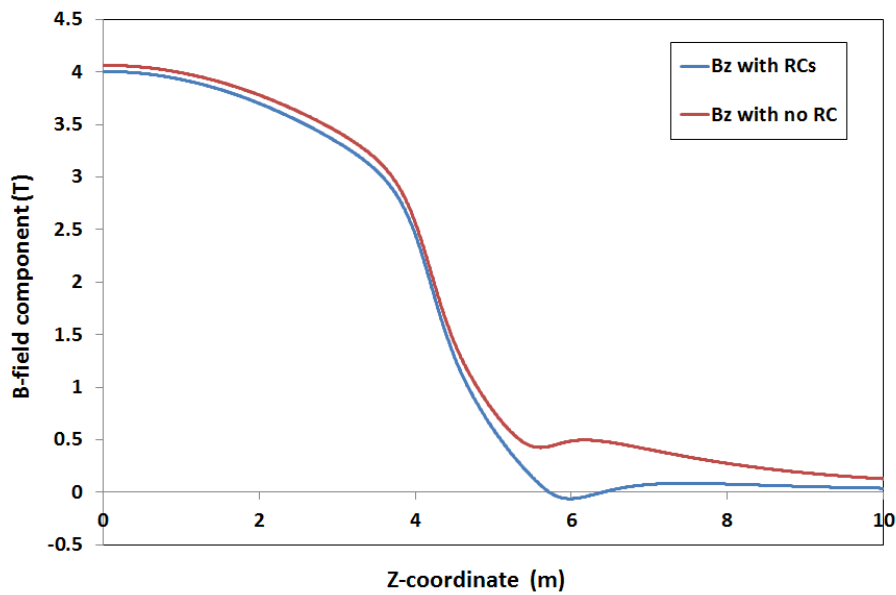[4]Note that these end coils are not part of the detector simulation model.

Figure 29: The longitudinal magnetic field on axis, with and without end coils (RCs). Note that the yoke endcap extends to z = 5.7 m.

muon system with 6 instead of 9 layers (as in the CDR) should therefore be sufficient, with an additional 7th layer in the barrel as close as possible to the coil. Similarly, [32] states that the performance for equidistant muon detection layers is very similar to the model chosen for the CDR, where three groups of three layers were proposed. The muon system layout in CLICdet is shown in Figure 30.

As in the CDR, the muon detection layers are proposed to be built as RPCs with cells of 30×30 mm^2 (alternatively, crossed scintillator bars could be envisaged). The free space between yoke steel layers is 40 mm, which is considered generous given present-day technologies for building RPCs. In analogy to CMS, the yoke layers and thus the muon detectors are staggered to avoid gaps (see Figure 2).
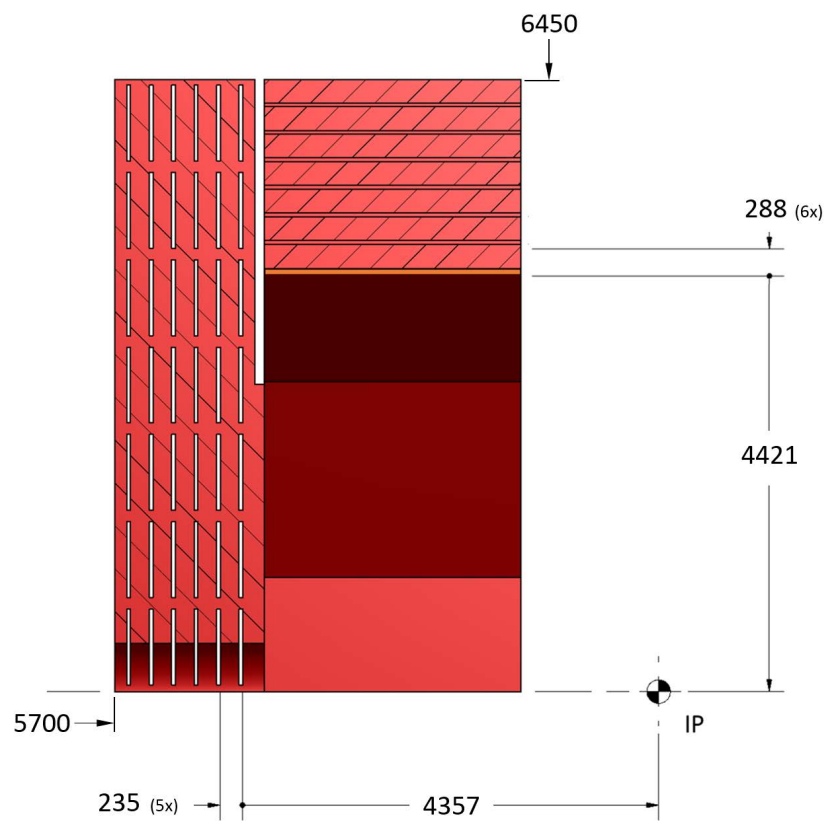
Figure 30: Schematic cross section of the muon system layout in the yoke of CLICdet. The staggering of the the layers is not visible in this cross section.

9   LumiCal, BeamCal and Intratrain Feedback

Two smaller electromagnetic calorimeters, LumiCal and BeamCal, are installed in the very forward region, on either side of the IP. Their specific purposes (luminosity measurement and monitoring of collisions) require that they are aligned with the outgoing beam axis. Moreover, these two calorimeters provide coverage for reconstructing electrons and photons down to very small angles. The positioning and overall dimensions of LumiCal and BeamCal are given in Table 18. Behind BeamCal, which acts as shielding for this more sensitive equipment, a beam position monitor (BPM) and kicker system for the intra-train feedback is installed. The basic design of the calorimeters and the feedback components remains as in CLIC_ILD. The positioning and radii of these elements are sligthly changed in the new detector model CLICdet.

9.1 Luminosity Calorimeter (LumiCal)

The main purpose of the LumiCal is the precise measurement of electrons and positrons from Bhabha scattering events. It consists of 40 layers of 3.5 mm tungsten and 0.32 mm silicon sensors. The segmentation of the sensor layers into sectors, and of these sectors into pads, is described in [33], however, due to its different longitudinal position in CLICdet, the LumiCal now has 64 radial and 48 azimuthal segments per layer. Each layer also contains 0.2 mm support (consisting of epoxy, kapton and copper) and 0.25 mm air gaps (see Table 19). The position and size of the LumiCal provide an overlap of the coverage with the ECAL endcap (see Figure 31).

9.2 Beam Calorimeter (BeamCal)

The BeamCal completes the coverage of the electromagnetic calorimeter down to 10 mrad (see Figure 31). Like the LumiCal, the BeamCal consists of 40 layers of 3.5 mm tungsten plates. The sensor material has to be radiation hard (up to 1 MGy per year), because the BeamCal has to absorb a large fraction of the incoherent electron-positron pairs from the beam-beam interaction. In the simulation 0.3 mm thick diamond layers are used as active elements. The BeamCal segmentation implemented in the software model of CLICdet consists of a regular pattern of 8×8 mm^2 cells. To reduce the number of particles scattering back into the detector, the side of the BeamCal facing the IP is covered with a 100 mm thick graphite layer. The layout as implemented in the simulation model is shown in Figure 31.

Table 18: Positioning and dimensions of LumiCal and BeamCal – the longitudinal dimension indicated for BeamCal includes the 100 mm of graphite absorber. The geometrical acceptance angles are given. In practice, the physical acceptance depends on shower containment. Note that LumiCal is partially in the shadow of the ECAL plug (see Figure 19).

	Z_{start} [mm]	Z_{end} [mm]	R_{in} [mm]	R_{out} [mm]	θ_{in} [mrad]	θ_{out} [mrad]
LumiCal	2539	2710	100	340	39	134
BeamCal	3181	3441	32	150	10	46

9.3 Intra-train Feedback

A system consisting of BPMs and fast kickers on either side of the interaction point is foreseen [34], allowing to partially correct luminosity loss due to vibrations and other imperfections. As schematically shown in Figure 31, these elements are placed as close as possible to the IP to reduce latency in the feedback. On the other hand, it is mandatory to install the BPM and kicker beyond BeamCal, which is acting as shielding for these elements as well as for the QD0. In the layout of CLICdet, the centre of the
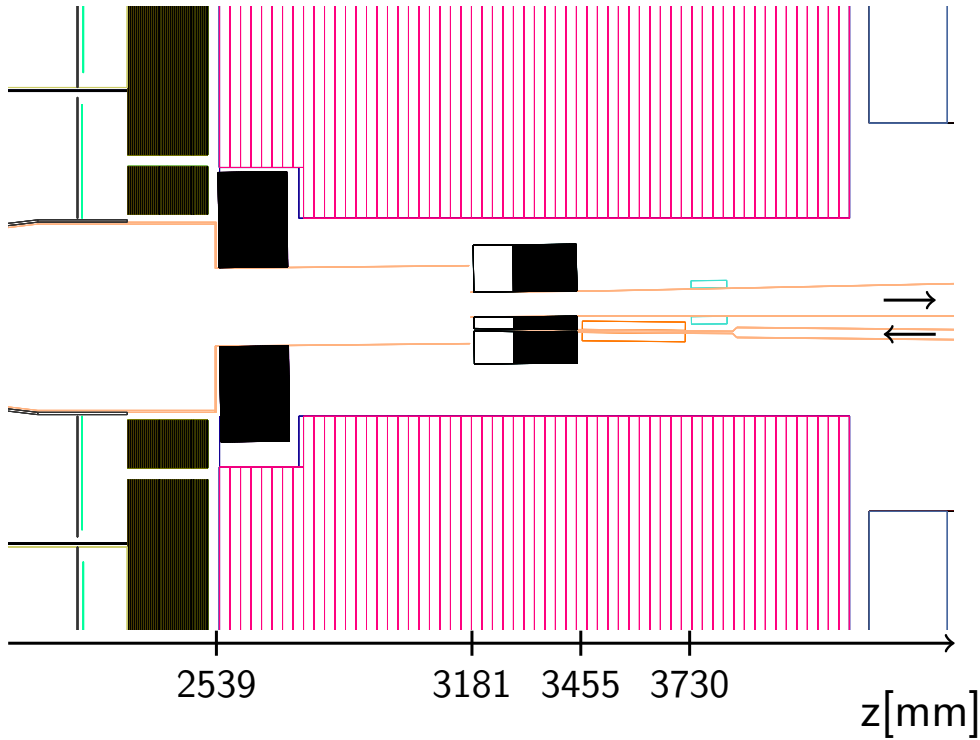
Figure 31: Layout of the forward region in CLICdet, seen from the top, as implemented in the simulation model. LumiCal and BeamCal are shown in black, a graphite absorber upstream of BeamCal (to reduce back-scattering) is shown in white. Downstream of BeamCal the kicker (on the incoming beam) and the beam position monitor (on the outgoing beam) are indicated. Both are components of the intra-train feedback system. The arrows indicate the direction of the beams.

Table 19: Parameters of the forward calorimeter layer structure. The number of layers N_{Layers}, their thickness d_{Layer}, the absorber material, its thickness d_{Abs}, the active material and its thickness d_{Act} are given.

	N_{Layers}	d_{Layer} [mm]	Absorber	d_{Abs} [mm]	Active	d_{Act} [mm]
LumiCal	40	4.27	Tungsten	3.5	Silicon	0.32
BeamCal	40	4.00	Tungsten	3.5	Diamond	0.30

BPM (installed on the outgoing beam, assumed to be 90 mm long) is located at 3775 mm from the IP. The centre of the kicker (on the incoming beam, assumed to be 260 mm long) is located at 3585 mm.

10 Beam Pipe and Vacuum System

The vacuum system in the detector is separated by valves from the accelerator vacuum (QD0 and beyond). A schematic view of the vacuum system is given in Figure 32, showing the thinner incoming and the larger outgoing beam pipes at the crossing angle of 20 mrad. The separating valves and additional pumping ports are considered part of the accelerator system and are not shown in the figure.

The main difference between this vacuum system layout and the one proposed in the CDR is the absence of a large vacuum valve just downstream of the LumiCal detector. The CDR layout was mainly motivated by the need for a rapid "push-pull" exchange of the detector on the IP, with little time for pumping the central region. However, without "push-pull" the rather modest requirements for the beam-line vacuum of about 10^{-6} mbar in the detector region imply that the full detector can be vented with dry nitrogen when an intervention (detector opening for maintenance) is needed.

Another difference concerns the beam pipe shapes and diameters: for the outgoing beam, the conical beam pipe in the region of BeamCal and BPM is replaced by a cylindrical pipe, and for the incoming beam, the cylindrical beam pipe has a larger diameter than in the CDR, making it less fragile. This is possible since, in the absence of QD0, more space is available inside the support tube.
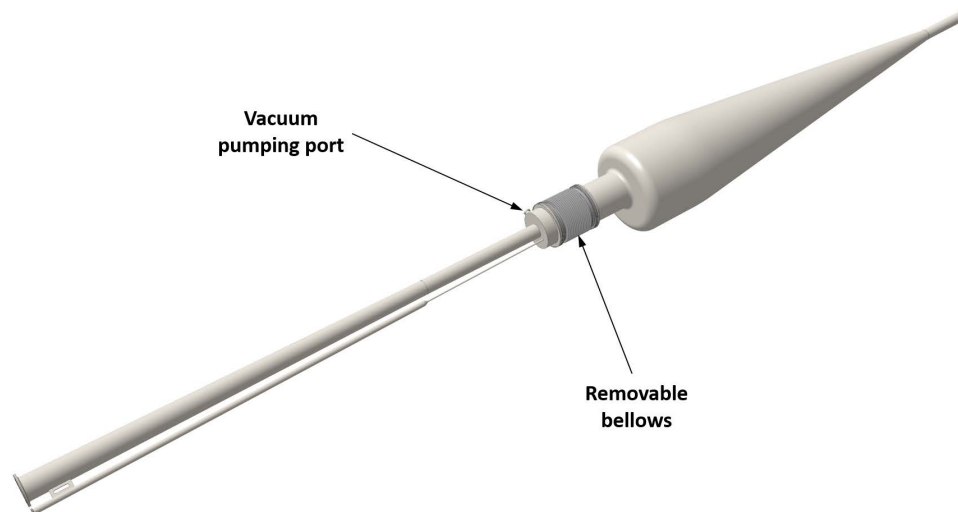

Figure 32: Schematic view of the components of the vacuum system in the detector region (the IP is located at the right hand edge of the figure).

The geometrical parameters of the different parts of the beam pipe as implemented in the simulation model are described in Table 20. Around the interaction point the beam pipe consists of a beryllium cylinder. The next part of the beam pipe is a steel cone with a half-opening of 6.6°. The wall thickness of this cone increases from 4 mm in the most central region to 4.8 mm in the region of largest diameter of the cone (engineering rule of thumb: the wall thickness should not be less than 1% of the diameter). The steel pipe acts as absorber for particles scattering back from the forward region [11]. The maximal cone radius is given by the inner radius of the ECAL endcap "plug". At a radius of 240 mm the beam pipe becomes cylindrical until it reaches the front face of the LumiCal.

Just upstream of the LumiCal, the beam pipe diameter is reduced from its full opening to fit the 100 mm inner radius of LumiCal, which is centred on the outgoing beam axis. The corresponding vertical end-flange is assumed to be 3 mm thick.

The beam pipe changes again before the BeamCal, when it splits into two separate pipes: A thin cylindrical beam pipe for the incoming beam, and a larger cylindrical beam pipe for the outgoing beam.

Table 20: Parameters for the beam pipe parts as implemented in the simulation model. Each part is a cylinder barrel or cone positioned between Z_1 to Z_2, the radii $R_{1/2}^{\text{In/Out}}$ are the inner and outer radii at position $Z_{1/2}$ respectively.

&[A]	Z_1 [mm]	Z_2 [mm]	R_1^{In} [mm]	R_2^{In} [mm]	R_1^{Out} [mm]	R_2^{Out} [mm]	Material
0	0	308	29.4	29.4	30.0	30.0	Beryllium
0	308	337	29.4	29.4	30.0	33.4	Iron
0	337	2080	29.4	235.2	33.4	240.0	Iron
0	2080	2528	235.2	235.2	240.0	240.0	Iron
0[B]	2528	2531	0.0	98.0	240.0	240.0	Iron
2	2531	3170	98.0	98.0	99.0	99.0	Iron
2[C]	3170	3173	2.7	31.0	99.0	99.0	Iron
2	3173	3500	31.0	31.0	32.0	32.0	Iron
2[D]	3500	12500	31.0	125.0	32.0	127.0	Iron
1	3173	3281	2.7	2.7	3.7	3.7	Iron
1	3281	3835	2.7	2.7	3.7	3.7	Iron
1	3835	3845	2.7	12.0	3.7	13.5	Iron
1	3845	12500	12.0	12.0	13.5	13.5	Iron

[A] Alignment of beam pipe part: 0 (aligned on detector axis), 1 (aligned on incoming beam axis), 2 (aligned on outgoing beam axis).

[B] Beam pipe end in front of LumiCal: R_1^{Out} is the size of the hole where the beam pipe inside LumiCal is connected. The hole is centred on the outgoing beam axis.

[C] Beam pipe end in front of BeamCal: R_1^{In} is the size of the hole for the incoming beam pipe, R_1^{Out} is the size of the hole for the outgoing beam pipe.

[D] Conical beam pipe with an half-opening angle of 10 mrad.

11 Detector Opening and Maintenance

The preliminary procedure for detector opening and maintenance, as outlined in the CDR, can be applied to CLICdet with minor changes. The main steps are:

- close all beam pipe vacuum valves, vent the beam pipe in the detector region with a dry gas (e.g. nitrogen);

- open the vacuum on the detector-side of QD0, close the detector vacuum system by flanges;

- move the detector from the IP to the garage position in the cavern;

- the support tube installation/extraction tool is installed behind the endcap;

- the jacks holding the support tube in position are retracted;

- the endcap is slid back, giving access to the vacuum connection between forward region and central detector;

- open vacuum connection near LumiCal, remove bellows as shown in Figure 33;

- LumiCal is opened sideways, and the support tube can be retracted some 50 cm by the extraction tool;

- close the vacuum system on all sides by flanges;

- remove the support tube as a whole by a crane;

In case the inner detector system needs to be extracted, both endcaps need to be opened as described above: On one side, the endcap needs to be retracted by 4–5 m to make space for a support platform. On the opposite side, the opening needs to be sufficient to disconnect the vacuum system at the level of the bellows near the LumiCal. Tooling and procedures needed to extract the inner detector system are currently under study.
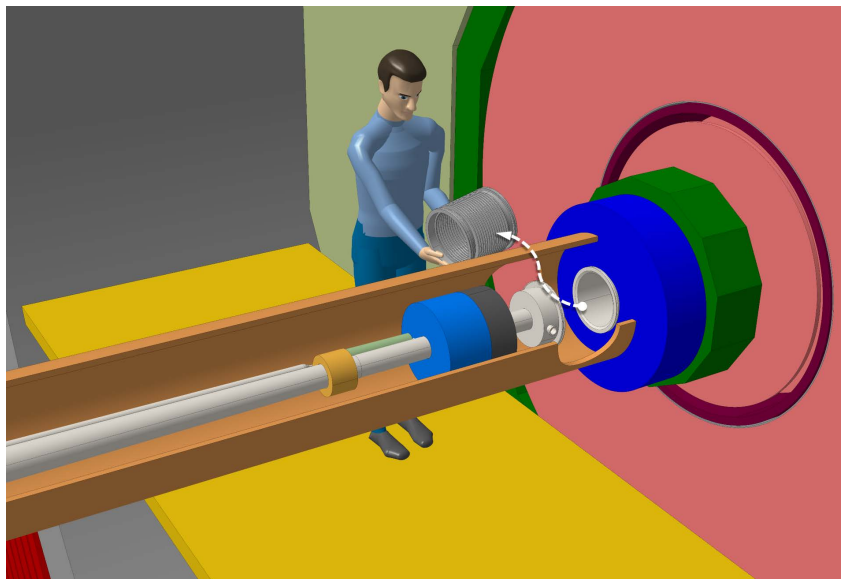

Figure 33: Removal of the bellows downstream of LumiCal.

12 Summary and Outlook

This note describes the new CLIC detector model, CLICdet, and all of its sub-systems in its version of spring 2017. This detector model has been implemented in the new, DD4hep-based CLIC detector software chain. The simulation and reconstruction processes are currently being finalized. Validation studies are ongoing, in view of physics benchmark studies with full detector simulations.

13 Appendix I

Table 21: Overview of CLICdet sub-detector parameters. Note that numbers for barrel detectors or disks contain the sum of both sides of the experiment.

Subdetector	Sensor area [m^2]	Cell size [mm^2]	Number of channels [10^6]
VTX barrel	0.487	0.025×0.025	780
VTX spirals	0.351	0.025×0.025	560
Inner Tracker Disk ITD1	1.26	0.025×0.025	2000
Inner Tracker Disk ITD2	2.26	0.05×1	46
Inner Tracker Disk ITD3	2.20	0.05×1	44
Inner Tracker Disk ITD4	2.06	0.05×1	42
Inner Tracker Disk ITD5	1.96	0.05×1	40
Inner Tracker Disk ITD6	1.88	0.05×1	38
Inner Tracker Disk ITD7	1.82	0.05×1	36
Outer Tracker Disk OTD1	13.92	0.05×10	27.8
Outer Tracker Disk OTD2	13.92	0.05×10	27.8
Outer Tracker Disk OTD3	13.92	0.05×10	27.8
Outer Tracker Disk OTD4	13.92	0.05×10	27.8
Inner Tracker Barrel ITB1	0.79	0.05×1	16
Inner Tracker Barrel ITB2	2.20	0.05×1	44
Inner Tracker Barrel ITB3	5.22	0.05×5	21
Outer Tracker Barrel OTB1	14.30	0.05×10	29
Outer Tracker Barrel OTB2	20.32	0.05×10	41
Outer Tracker Barrel OTB3	26.04	0.05×10	52
ECAL barrel	1808	5×5	72
ECAL endcaps (incl. ECAL plugs)	726	5×5	29
HCAL barrel	4346	30×30	4.8
HCAL endcaps	4041	30×30	4.5
HCAL rings	340	30×30	0.4
MUON barrel	1942	30×30	2.2
MUON endcaps	1547	30×30	1.7
LumiCal	26.5	3.75×(13 – 44)	0.25
BeamCal	5.4	8×8	0.093

14 Appendix II

Table 22: Pandora parameters and software versions used to produce the results shown in Figures 18 and 19 [22].

HCAL Timing Cuts	100 ns
ECAL Timing Cuts	100 ns
HCAL Hadronic Cell Truncation	1 GeV (Optimal for Default HCAL)
Software	ilcsoft_v01-17-07, including PandoraPFA v02-00-00
Digitiser	ILDCaloDigi, realistic ECAL and HCAL digitisation options enabled
Calibration	PandoraAnalysis toolkit v01-00-00

Table 23: Pandora parameters and software versions used to produce the results shown in Figures 20 and 21 - from [35].

Detector model	CLIC_o3_v06
HCAL Timing Cuts	10 ns
ECAL Timing Cuts	10 ns
HCALHadronic Cell Truncation	1 GeV (Optimal for Default HCAL)
Software	simulation DD4hep 0.18, iLCSoft package from CLICdp builds 2016-11-09
Reconstruction	DDMarlinPandora, using PandoraPFA v03-00-00
Digitiser	DDMarlinCaloDigi, realistic ECAL and HCALl digitisation options NOT enabled
Calibration	PandoraAnalysis toolkit v01-00-00

15 Appendix III

List of changes introduced on 5 April 2019:

- numbers in Appendix I were corrected and LumiCal / BeamCal numbers added;

- the present layout of LumiCal, i.e. 64 radial and 48 azimuthal segments per layer, was added in section 9.1.

References

[1] A. Munnich A., A. Sailer,
The CLIC-ILD-CDR Geometry for the CDR Monte Carlo Mass Production
(2011), LCD-Note-2011-002.

[2] C. Grefe, A. Munnich,
The CLIC-SiD-CDR Detector Model for the CLIC CDR Monte Carlo Mass Production
(2011), LCD-Note-2011-009.

[3] L. Linssen et al., eds., *Physics and Detectors at CLIC: CLIC Conceptual Design Report*,
vol. CERN-2012-003, 2012.

[4] CLIC, CLICdp, *Updated baseline for a staged Compact Linear Collider*, CERN-2016-004,
CERN, 2016.

[5] M. Regler, et al., *LiC Detector Toy, Vienna Fast Simulation Tool for Charged Tracks*,
http://www.hephy.at/project/ilc/lictoy/.

[6] T. Behnke, et al.,
The International Linear Collider Technical Design Report - Volume 4: Detectors,
CERN-ATS-2013-037, 2013.

[7] M. Killenberg, *Occupancy in the CLIC ILD Time Projection Chamber*
(2011), LCD-Note-2011-029.

[8] M. Killenberg, *Occupancy in the CLIC ILD Time Projection Chamber using Pixelised Readout*
(2013), LCD-Note-2013-005.

[9] M. Thomson, *Particle Flow Calorimetry and the PandoraPFA Algorithm*,
Nucl. Instrum. Meth. **A 611** (2009) 25.

[10] R. Gluckstern, *Uncertainties in track momentum and direction, due to multiple scattering and measurement errors*, Nucl. Instrum. Meth. **24** (1963) 381.

[11] D. Dannheim, A. Sailer, *Beam-Induced Backgrounds in the CLIC Detectors*
(2011), LCD-Note-2011-021.

[12] N. Alipour Tehrani, *Optimisation studies for the CLIC vertex-detector geometry*
(2015), CLICdp-Conf-2015-002.

[13] A. Herve, *Different presentations on design and costing of superconducting magnet systems for experiments*, https://edms.cern.ch/document/1740563/, 2008 - 2010.

[14] B. Parker et al., *Functional Requirements on the Design of the Detectors and the Interaction Region of an e+e- Linear Collider with a Push-Pull Arrangement of Detectors*
(2009), ILD-Note-2009-050.

[15] F. Kircher et al., *Conceptual Design of the ILD Detector Magnet System*
(2012), LC-DET-2012-081.

[16] A. Bartalesi, M. Modena,
3D FEA Computation of the CLIC Machine Detector Interface Magnets (2012).

[17] F. Duarte Ramos, H. Gerwig, M. Villarejo Bermudez, *CLIC inner detectors cooling simulations*
(2013), LCD-Note-2013-007.

[18] N. Alipour Tehrani, P. Roloff, *Optimisation Studies for the CLIC Vertex-Detector Geometry*
(2014), CLICdp-Note-2014-002.

[19] S. Sroka et al., *New CLIC detector model - engineering input to the vertex and tracker layout*,
EDMS document No. 1706383, 2016.

[20] F. Duarte Ramos, W. Klempt, F.-X. Nuiry,
Experimental tests on the air cooling of the CLIC vertex detector
(2015), CLICdp-Note-2016-002.

[21] M. Villarejo Bermudez, F. Duarte Ramos, H. Gerwig,
Mechanical integration studies for the CLIC vertex and inner tracking detectors
(2015), CLICdp-Note-2015-002.

[22] S. Green, J. S. Marshall, B. Xu, *private communication*, 2016.

[23] P. Roloff, *Photon reconstruction requirements*,
presentation at the ECFA Linear Collider workshop 2016, Santander, Spain,
https://agenda.linearcollider.org/event/7014/contributions/34682/.

[24] S. Poss, A. Sailer, *Luminosity Spectrum Reconstruction at Linear Colliders*,
EPJC **74** (2014) 2833.

[25] N. Nikiforou, M. Weber, *Update on ECAL photon performance / optimisation*,
presentation at the ECFA Linear Collider Workshop 2016, Santander, Spain,
https://agenda.linearcollider.org/event/7014/contributions/34659/.

[26] M. Reinhard, *CP violation in the Higgs sector with a next-generation detector at the ILC*,
PhD thesis, École polytechnique Laboratoire Leprince-Ringuet, 2009.

[27] N. Nikiforou, *Hadronic Calorimeter Optimization for a New Detector Model at CLIC*
(2016), Draft Note, https://edms.cern.ch/document/1756529/.

[28] L. Linssen et al., eds., *Physics and Detectors at CLIC: CLIC Conceptual Design Report, Fig. 6.2*,
vol. CERN-2012-003, 2012.

[29] S. van Dam, A. Sailer, *The occupancy in the Hadronic Calorimeter endcap of the CLIC detector*
(2014), CLICdp-Note-2014-004.

[30] B. Dalena, D. Schulte, R. Thomas, *Impact of the Experiment Solenoid on the CLIC Luminosity*
(2010), CERN-ATS-2010-081.

[31] H. Gerwig, A. Herve, *Ring Coils on the Endcap Yoke of a CLIC Detector*
(2011), LCD-Note-2011-017.

[32] E. van der Kraaij, B. Schmidt, *Muon System Design Studies for Detectors at CLIC*
(2011), LCD-Note-2011-008.

[33] H. Abramowicz et al., *A Luminosity Calorimeter for CLIC* (2009), LCD-Note-2009-002.

[34] J. Resta-Lopez, P. N. Burrows, G. Christian, *Luminosity Performance Studies of the Compact Linear Collider with Intra-train Feedback System at the Interaction Point*,
JINST **5** (2010) 09007.

[35] M. Weber, *Update on ECAL photon optimisation*, presentation at the CLICdp working group on detector optimisation, CERN, Switzerland, https://indico.cern.ch/event/581371/.